

# The Future of Ultra Wideband Systems in Medicine: Orthopedic Surgical Navigation

Mohamed Mahfouz, Michael Kuhn and Gary To  
*University of Tennessee,  
United State of America*

## 1. Introduction

Ultra-wideband (UWB) technology has been utilized in low probability of detection radar and communications systems for decades since its inception from time domain electromagnetics in the 1960s (Fontana, 2004). Interest in UWB for unique indoor communications and positioning applications has skyrocketed since the FCC released its notice of inquiry in 1998 and then opened up the 3.1-10.6 GHz and 22-29 GHz frequency bands for UWB use in 2002 (FCC, 2002).

### 1.1 General overview of ultra-wideband technology for indoor positioning systems

A depiction of a typical indoor positioning system is shown in Figure 1 where the base stations are connected to a master processing unit, and a reference tag is needed to bring the mobile tag into the 3-D global coordinate frame. The use of time difference of arrival for 3-D triangulation combined with leading-edge detection at the UWB receiver help mitigate the stringent requirements needed in terms of base station synchronization and ranging sensitivity to dense indoor multipath interference. Although the system architecture shown in Figure 1 is well known and has been implemented in other wireless positioning systems including GPS, realizing this architecture for high accuracy indoor 3-D positioning has proven to be deceptively difficult.

Central difficulties in achieving high 3-D real-time accuracy for indoor localization systems include indoor multipath interference, sampling-rate limitations, local oscillator phase noise, phase center effects, system clock jitter and drift, etc. Many techniques have been proposed for ranging in UWB positioning systems which includes (see Figure 2a): leading-edge detection (Fontana, 2004), matched filter (Low et al., 2005), received signal strength (Ekahau Inc, 2008), first peak detect (Alavi & Pahlavan, 2006), and peak search and subtract (Falsi et al., 2006). The main limitation of peak detection algorithms (e.g. received signal strength, first peak detect, and peak search and subtract) is assuming *a priori* information concerning the received pulse shape. The matched filter is useful in low signal-to-noise ratio (SNR) environments in conjunction with leading-edge detection. In realistic indoor environments which contain significant multipath interference, this introduces large 1-D ranging errors resulting in poor overall 3-D accuracy (Figure 2b). In many current systems, a tunnel (or square law) diode is used at the receiver for energy detection which integrates a nanosecond of the incoming signal, putting an upper bound of roughly 5 cm on the 1-D ranging

accuracy even when using leading-edge detection (Fontana, 2004). The ranging limitations due to multipath interference are compounded with sampling rate limitations. The use of conventional analog-to-digital converters (ADC), even if 5-10 GSPS, places an upper bound on the 1-D ranging accuracy of 5 cm.

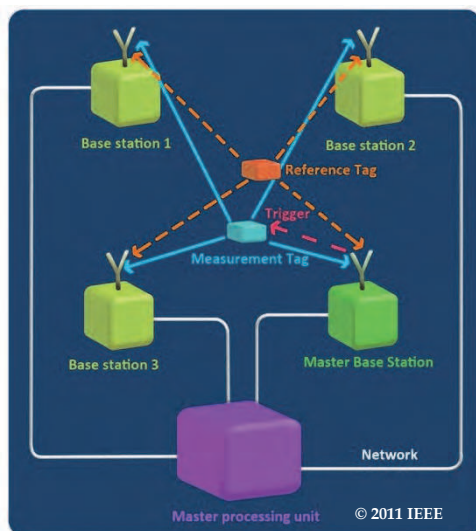


Fig. 1. A typical indoor positioning system where four or more base stations triangulate the 3-D position of a mobile tag, and a reference tag in a known location serves as a reference point for the global coordinate frame (Mahfouz, Kuhn, Wang et al., 2011).

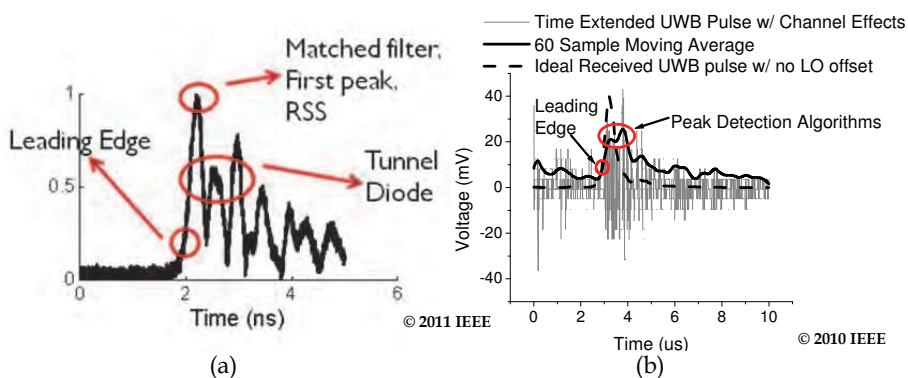


Fig. 2. (a) Comparison of peak and leading-edge detection methods utilized at the UWB receiver where the leading-edge of the multipath signal provides the highest accuracy and does not assume *a priori* pulse shape information (Mahfouz, Kuhn, Wang et al., 2011), (b) received signal where significant pulse distortion causes noticeable error in locating the correct peak position while the leading-edge of the UWB pulse results in mm 1-D ranging (Kuhn et al., 2010).

### 1.1.1 Commercial systems

As shown in Table 1, current commercial UWB systems can achieve 3-D localization accuracy in the range of 15 – 30 cm. A comparison of the DART Ultra-Wideband system from Zebra Enterprise Solutions and the real-time location system (RTLS) from Ubisense is given in Table 1 (Zebra Enterprise Solutions, 2011, Ubisense, 2011). As shown in Table 1, the two systems share many commonalities including frequency range, operating range, compact tag size, and overall 3-D accuracy. One major difference is the method of digital communication: the Zebra Enterprise Solutions system uses UWB pulse-based modulation whereas the Ubisense system uses a narrowband 2.4 GHz digital communication scheme. Although 2.4 GHz communication is a more mature technology than UWB pulse-based modulation, it has a distinct disadvantage in that it is much more susceptible to multipath interference and may experience severe degradation depending on the operating environment of the system. Figure 3 shows the two commercial systems. The Zebra Enterprise Solutions system is shown in Figure 3a including the main controller and four hubs while Figure 3b shows two different sized tags from the Ubisense RTLS.

| Company                    | Frequency Range (GHz) | Operating Range (m) | Tag Size (cm <sup>3</sup> )    | Number of Tags | Refresh Rate (Hz) | Localization Method | Accuracy (cm) |
|----------------------------|-----------------------|---------------------|--------------------------------|----------------|-------------------|---------------------|---------------|
| Zebra Enterprise Solutions | 5.94 - 7.12           | > 50                | 1.12x<br>4.01x<br>2.11<br>3.8x | 10,000         | <1-100            | TDOA                | < 30          |
| Ubisense                   | 5.8 - 7.2             | > 50                | 3.9x<br>1.65                   | > 1000         | <1-34             | TDOA and AOA        | < 15          |

Table 1. Comparison of commercial UWB localization systems with specifications of their compact tags.

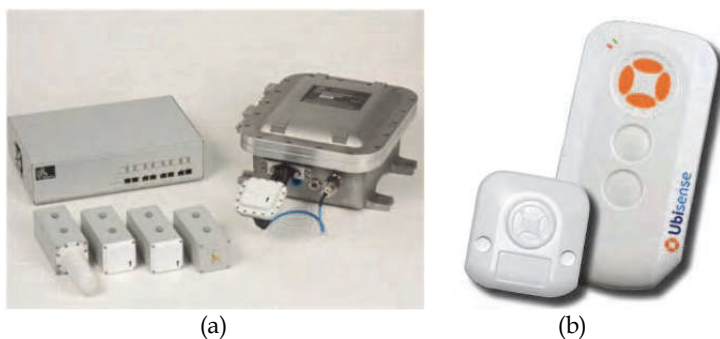


Fig. 3. Commercial indoor UWB localization systems (a) Zebra Enterprise Solutions, (b) Ubisense.

### 1.1.2 Research systems

Competing technologies for high accuracy indoor positioning include frequency modulated continuous wave (FMCW), impulse-based (i.e. carrier-free) UWB, and carrier-based UWB.

Table 2 provides a summary of the various research groups utilizing these three approaches for high accuracy indoor positioning. Similar accuracy levels (0.5-20 cm) have been achieved for both carrier-based (Meier, 2007; Mahfouz, 2008; Zhang, 2010; Waldmann, 2008; McEwan, 2004) and impulse-based (Low, 2005; Zetik, 2004; Ossberger, 2004; Fujii, 2007) UWB positioning systems, although carrier-based systems have shown the potential for mm and sub-mm range accuracy even for 3-D indoor environments (Mahfouz, 2008; Zhang, 2010; Meier, 2007; McEwan, 2004). FMCW has proven to be a successful competing technology for high accuracy positioning systems (Stelzer, 1999, 2004; Ellinger, 2007; Mosshammer, 2007; Tragas, 2007; Feger, 2009). In the 5.8 GHz band for industrial, medical, and scientific (ISM) applications, documented accuracy of 5-20 cm for 2-D has been achieved (Stelzer, 2004; Ellinger, 2007; Mosshammer, 2007; Tragas, 2007). FMCW systems operating at higher frequencies including 35 GHz and 77 GHz have achieved accuracy levels of 0.1 mm (Stelzer, 1999, Feger, 2009) with the system described by Feger et al. working at ranges of up to 10 m (Feger, 2009). The most recent FMCW trend is a European-wide push to create low power wireless sensor networks built on 5.8 GHz FMCW technology (Ellinger, 2007; Mosshammer, 2007; Tragas, 2007; Feger, 2009).

### 1.1.3 Available frequency bands

Wireless medical devices, for both positioning and communication, have stringent requirements on the frequency bands in which they can operate. Table 3 highlights the different bands both in the United States and Europe which can be used for indoor medical applications for both narrowband and UWB applications. UWB has available frequency bands from 3.1 – 10.6 GHz and 22 – 29 GHz in the U.S. Only portions of that 3.1 – 10.6 GHz band are currently available in Europe. A number of telemetry bands exist in the U.S., and both the U.S. and Europe have instrumentation, scientific, and medical (ISM) bands available, mainly in the 300 MHz to 3 GHz range. As shown in Table 3, *in vivo* telemetry applications typically use bands in the RF and lower microwave frequency range for operation (i.e. 315 MHz, 402 – 405 MHz, and up to 1427 – 1432 MHz in the United States while Europe uses 433.05 – 434.79 MHz and 868 – 870 MHz). In order to understand why telemetry bands are not allocated above 1.43 GHz, it is necessary to look at the complex permittivity of human tissues as done in Section 1.2.1, where losses greatly increase above 1 GHz. The UWB positioning system operates from 5.4 – 10.6 GHz in the upper region of the 3.1-10.6 GHz band while most wireless telemetry systems for *in vivo* operate at 433.92 MHz in the 433.05 - 434.79 European ISM band and at 315 MHz for the U.S. ISM band. As shown in Figure 4, the allocated band in the United States goes from 3-10.6 GHz at a power level of -41.3 dBm/MHz. Compared to Europe, where the power level is required to be at -71.3 dBm/MHz from 4.8-6 GHz, -65 dBm/MHz from 8.5-10.6 GHz, and can only be at -41.3 dBm/MHz from 3.4-4.8 GHz if detect and avoid (DAA) circuitry is implemented to minimize interference with other wireless systems operating in this band. Figure 5 compares the UWB bands in Japan versus the United States. Similar to Europe, the Japanese regulations also require DAA in the 3.4-4.8 GHz band. The main difference between the European band and the Japanese band is in the no DAA band: in Europe, this exists from 6-8.5 GHz while in Japan, this band goes from 8.5-10.6 GHz. From looking at Figure 4 and Figure 5, it is clear that the various restrictions imposed around the world make designing one system for worldwide operation difficult to achieve. Multiple variations of a system may be needed to meet the various worldwide regulations.

| Research Group/<br>Company            | System Architecture        | Frequency<br>(GHz) | Reported<br>Error | Operating Range |
|---------------------------------------|----------------------------|--------------------|-------------------|-----------------|
| Mahfouz, 2009                         | Carrier-Based UWB          | 5.4-10.6           | 2-5 mm (3-D)      | 5 m/ Indoor     |
| Waldmann, 2008                        | Carrier-Based UWB          | 7-8                | 1.7 cm (1-D)      | 10 m/ Indoor    |
| Meier, 2007                           | Carrier-Based UWB          | 22.58-25.7         | 0.1-2 mm (1-D)    | 8 m/ Indoor     |
| McEwan, 2004                          | Carrier-Based UWB          | 5.8                | < 2 mm (2-D)      | 10 cm x 10 cm   |
| Ossberger, 2004                       | Impulse-Based UWB          | ~2-7               | 5-10 mm (1-D)     | 5 m/ Indoor     |
| Fujii, 2007                           | Impulse-Based UWB          | 3.7-5              | 20 cm (2-D)       | 8 m/ Indoor     |
| Low, 2005                             | Impulse-Based UWB          | 3.2-5.2            | 1 cm (1-D)        | 8 m/ Indoor     |
| Zetik, 2004                           | Impulse-Based UWB          | 0.01-5             | 1.5 cm (2-D)      | 2 m/ Indoor     |
| Stelzer, 1999                         | FMCW and<br>Interferometry | 35                 | 0.1 mm (1-D)      | < 1 m/ Indoor   |
| Stelzer, 2004                         | FMCW                       | 5.8                | 10 cm (2-D)       | 500 m/ Outdoor  |
| Ellinger, 2007<br>Mosshammer,<br>2007 | FMCW                       | 5.8                | 18 cm (2-D)       | 40 m/ Indoor    |
| Feger, 2009                           | FMCW                       | 77                 | 0.1 mm (1-D)      | 1.5 m/ Chamber  |

Table 2. Comparison of current research high accuracy positioning systems.

| Location | Frequency Band                                 | Frequency (MHz)  |
|----------|--|--|
| U.S.     | Medical Implant Communications Service         | 402 - 405  |
| U.S.     | Wireless Medical Telemetry Service             | 608 - 614; 1395 - 1400; 1427 - 1432                    |
| U.S.     | Instrumentation, Scientific, and Medical (ISM) | 315; 902 - 928; 2400 - 2483.5; 5150 - 5875             |
| Europe   | ISM  | 433.05 - 434.79; 868 - 870 (short-range) 2400 - 2483.5 |
| U.S.     | UWB  | 3.1 - 10.6 GHz; 22 - 29 GHz, center freq > 24.075 GHz  |
| Europe   | UWB  | 3.4 - 4.8 GHz; 6 - 8.5 GHz                             |
| Japan    | UWB  | 3.4 - 4.8 GHz; 8.5 - 10.6 GHz                          |

Table 3. Summary of licensed medical wireless frequency bands.

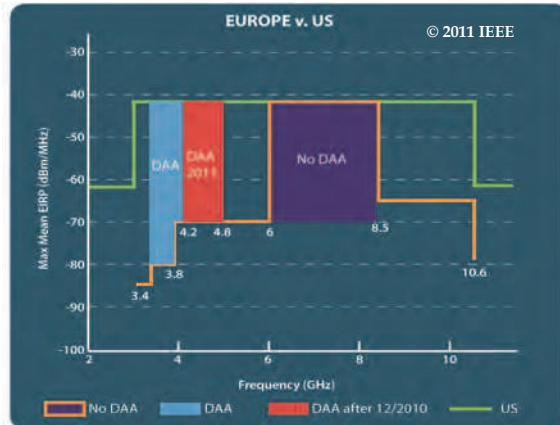


Fig. 4. Comparison of allocated UWB bands between 3-11 GHz in the U.S. versus Europe (Mahfouz & Kuhn, 2011).

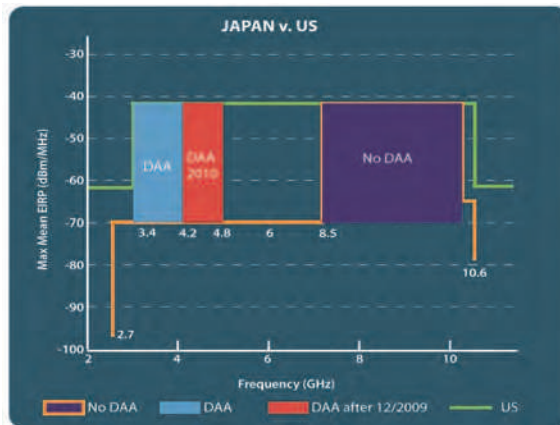


Fig. 5. Comparison of allocated UWB bands between 3-11 GHz in the U.S. versus Japan.

**1.2 Microwave interaction with biological tissues**

The electrical characteristics of biological tissues change dramatically from DC through higher frequencies such as X-ray and gamma radiation. At very low frequencies (the kHz range), the primary means through which electrical current travels through the body is conduction via the extracellular matrix. At the visible frequency range and even higher in ultraviolet (UV) and X-ray frequency ranges, most electromagnetic waves are able to pass through biological tissues, with differing amounts of energy being absorbed by different tissues. Between these two extremes lie the RF/Microwave frequency bands. Electrical properties of biological tissues change dramatically over this frequency range. There are specific techniques, such as coaxial probe dielectric measurements, which can be followed to apply a uniform method for electrical characterization of biological tissues (or other lossy media) over this frequency range.

RF/Microwave radiation is considered from 100 kHz – 300 GHz. Although the interaction of radiation with biological tissues changes significantly over this range, there are some similar properties that provide coherence for grouping RF/Microwave frequencies together. First, over this whole frequency range radiation can be considered non-ionizing. Ionizing radiation includes UV and X-ray, and these frequency ranges are characterized by disruption of atomic structures. Second, it is convenient and useful to use RF/Microwave frequencies for the purpose of radiating electromagnetic (EM) energy. At low frequencies (LF) and extremely low frequencies (ELF), the wavelength of the transmitting signal is much larger than the structures used in transporting it. Radiation at LF and ELF is not typically seen. Conversely, the wavelengths in the RF/Microwave range are comparable to their corresponding transmission lines (millimeter to meter in size), which makes them ideal for radiation applications. Central to designing a microwave system which utilizes biological tissues as a transmission medium is a thorough understanding of the electrical properties of the tissues that will be exposed to the EM energy. An enormous amount of research has been done in this area. This has included use of a wide range of measurement techniques, testing on many different types of animals as well as humans, and testing of biological tissues in different environments (e.g. *in vivo*, *in vitro*, over a range of temperatures, etc.).

### 1.2.1 Complex permittivity

The complex permittivity is a common method used to characterize the electrical properties of an arbitrary medium. Combined with other electrical parameters, such as conductivity and skin depth, it can be used to provide complete electrical characterization. (1) shows the basic definition of complex permittivity

$$\varepsilon^* = \varepsilon' - j\varepsilon'' \quad (1)$$

where the first term,  $\varepsilon'$ , represents the capacitive nature of the tissue (amount of charge stored in it) while  $\varepsilon''$  characterizes the lossy nature of the medium. Using these two terms, it is possible to calculate  $\alpha$  and  $\beta$ , which can then be used to characterize how an EM wave behaves inside the medium (Vorst, 2006). (2) defines the loss tangent  $\tan\delta$  where  $\omega$  is the angular frequency,  $\sigma$  is the conductivity, and  $\varepsilon', \varepsilon''$  are defined in (1). (3) describes how to calculate  $\alpha$  and  $\beta$  using the wavelength in free space  $\lambda_0$ ,  $\tan\delta$  is the loss tangent, and  $\varepsilon'$  is the relative permittivity. (4) shows how the time and distance varying electrical field  $E(z, t)$  is calculated using  $\alpha$  and  $\beta$ .

$$\tan \delta = \frac{\omega\varepsilon'' + \sigma}{\omega\varepsilon'} \quad (2)$$

$$\alpha = \frac{2\pi}{\lambda_0} \sqrt{\frac{\varepsilon'}{2}(\sqrt{1 + \tan^2 \delta} - 1)}$$

$$\beta = \frac{2\pi}{\lambda_0} \sqrt{\frac{\varepsilon'}{2}(\sqrt{1 + \tan^2 \delta} + 1)} \quad (3)$$

$$E(z, t) = E_0 e^{j\omega t - (\alpha + j\beta)z} \quad (4)$$

Finally, the power dissipated through the region can be calculated with the electric field

$$P = |E(z)|^2 \sigma \quad (5)$$

where  $E(z)$  only depends on spatial variation and  $\sigma$  is the conductivity of the medium. Estimating the power dissipated provides a key metric in designing microwave systems which utilize biological tissues as the propagation medium. The electrical losses can be attributed to both ionic conduction and dipole rotation (Nelson, 1991)

$$\varepsilon'' = \varepsilon''_d + \varepsilon''_c \quad (6)$$

where  $\varepsilon''_d$  is loss from dipole rotation and  $\varepsilon''_c$  is the loss from ionic conduction. The standard way to model the complex permittivity for an arbitrary material is through the Cole-Cole equation

$$\varepsilon(w) = \varepsilon_\infty + \frac{\Delta\varepsilon}{1 + (j\omega\tau)^{1-\alpha}} \quad (7)$$

where there is a dispersion peak in the loss factor whose size and place depends on the relaxation time,  $\tau$ , and dispersion factor  $\alpha$ . Figure 6 shows typical curves for the complex permittivity of human tissues as modeled through the Cole-Cole equation (7) (Gabriel et al., 1996). A multi-peak Cole-Cole equation (8) is used by Gabriel et al. and allows a parametric model for complex permittivity to be established where multiple dispersion peaks and relaxation times are taken into account (Gabriel et al., 1996).

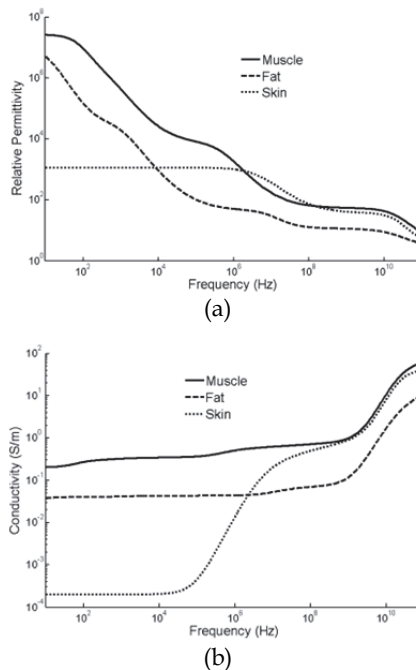


Fig. 6. Electrical properties of human muscle, fat, and skin at 37°C. (a) relative permittivity, (b) conductivity.

$$\varepsilon(w) = \varepsilon_{\infty} + \sum_{i=1}^4 \frac{\Delta\varepsilon_i}{1 + (j\omega\tau_i)^{1-\alpha_i}} + \frac{\sigma_{ionic}}{j\omega\varepsilon_0} \quad (8)$$

The loss factor in an arbitrary medium (i.e.  $\varepsilon''$ ) is due to both ionic conductivity and dipole rotation, and dipole rotation is the primary means through which losses occur over the RF and microwave frequency range. The various losses experienced through the microwave frequency range are shown in Figure 7. The temperature increases the ionic conductivity, which is the main reason the loss factor tends to increase with increases in temperature over lower microwave frequency range (DC - 1 GHz) (Komarov, Wang, & Tang, 2005). Above 1 GHz, the effects due to ionic conductivity lessen, and the loss factor is primarily due to dipole rotation (or free-water dispersion). This has the effect of decreasing the loss factor of water-based tissues, at least over the range of 3 - 17 GHz, with increase in temperature. Figure 8 shows how changes in temperature affect both  $\varepsilon'$  and  $\varepsilon''$  for water over a range of frequencies and temperatures (Komarov, Wang, & Tang, 2005). As Figure 8 shows in a qualitative sense, over the microwave frequency range of interest (3-17 GHz), increases in temperature tend to decrease  $\varepsilon'$  by an almost consistent amount (decrease of  $\sim 8$  for an increase in temperature of 25°C) and also tend to decrease  $\varepsilon''$ .

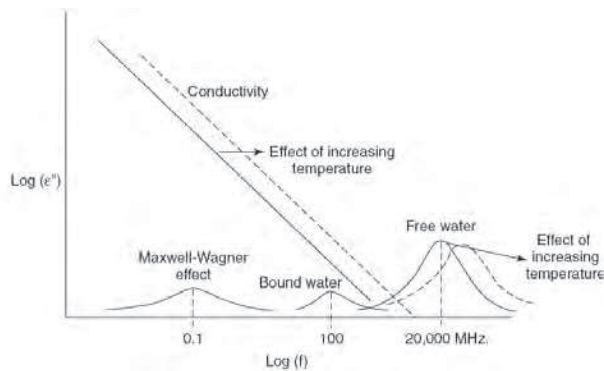


Fig. 7. Water and temperature effects on the loss factor (Komarov, Wang, & Tang, 2005)

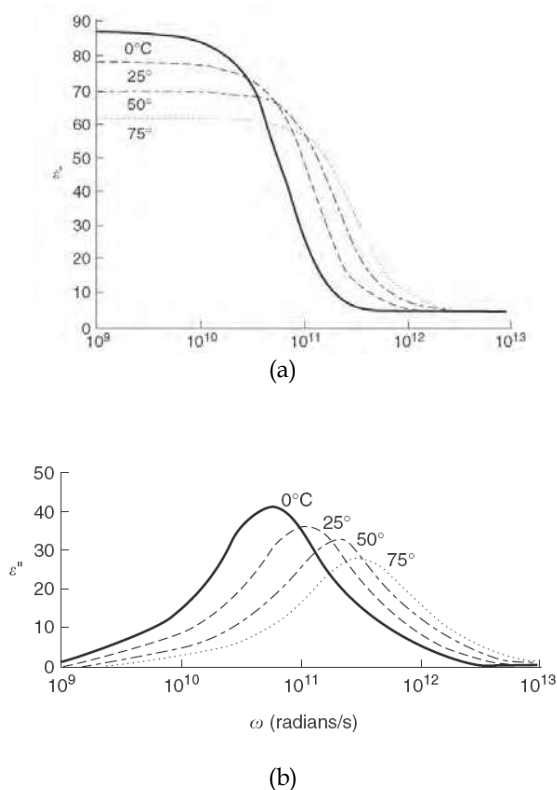


Fig. 8. Effects of temperature on complex permittivity of water: (a)  $\epsilon'$ , (b)  $\epsilon''$  (Komarov, Wang, & Tang, 2005)

Since most biological tissues are highly water-based, especially muscle and liver, they tend to follow similar trends for variation of complex permittivity over a range of temperatures. The change in complex permittivity of water is mostly due to the change in viscosity that occurs in water for varying temperatures. For example, a 32.4% decrease in viscosity of water is observed when going from 20°C to 37°C. This causes a decrease in the relaxation time  $\tau$  of approximately 38.2%.

## 2. State-of-the-art in wireless medical systems

The introduction of reliable low cost wireless technologies has significantly changed the medical industry over the past decade. There is a great demand for wireless medical equipment, most noticeably in the patient monitoring and personal health care. The primary reason for migrating from wired tools to wireless solutions is to eliminate the clumsy and restrictive wirings. It improves the overall efficiency by allowing multiple medical equipments to be controlled and monitored wirelessly by one single terminal device. The following sections illustrated a few of the commercially available wireless medical devices, as well as a number of researches being conducted.

## 2.1 Commercial devices

Vital signs monitoring devices are the most common medical systems being implemented with wireless technologies. Wireless blood pressure monitoring systems shown in Figure 9 can be used either in doctor office or for personal health monitoring. The wireless blood pressure cuff, as shown in Figure 10, was developed by SunTech and the Harvard Sensor Network Labs. They can be used by paramedics while responding to emergency. Wireless Oximeter (Figure 11) can measure the blood oxygen level of the patient up to 120 hours continuous monitoring from a fully charged battery. Figure 12 shows a wireless ECG monitoring device. It supports up to 12 channels and can be used continuously for 24 hours on a fully charged battery. This particular device demonstrates one of the great improvements for wireless medical system, which is enhancing the mobility of the patients. It allows nonstop monitoring of the patients' ECG and eliminates the need to attach and removing the ECG electrodes while being transferred around the hospital. A wireless EEG headset is shown in Figure 13. The current system support 14 sensors and can be used up to 12 hours on a full battery.



Fig. 9. Wireless blood pressure measuring device (Panasonic (n.d)).



Fig. 10. Wireless blood pressure cuff (SunTech (n.d)).



Fig. 11. Wireless Oximeter (Nonin (n.d)).



Fig. 12. Wireless ECG monitoring system (Life Science Corp (n.d)).



Fig. 13. Wireless EEG headset (Emotiv (n.d)).

While the devices mentioned above are used primary in hospital, there is also a great effort to develop personal healthcare devices to improve the quality of life of the patients. Devices such as glucometer, insulin pump and alcoholmeter have also been incorporated wirelessly with personal mobile devices (Figure 14 - Figure 16). In the recent years, a lot of focus has been given to minimally invasive methods to collect data for diagnosis. One of the most popular solutions to collect information within the gastrointestinal (GI) track is to use capsule camera as shown in Figure 17. The images taken are transmitted wirelessly to a computer to process. The capsule has also demonstrated the capability of producing images to help with diagnosis that cannot be accomplished with ordinary endoscopy and radiological methods.



Fig. 14. Wireless glucometer (Myglucometer (n.d)).



Fig. 15. Wireless insulin pump manager (Omnipod (n.d)).



Fig. 16. Wireless alcoholmeter (Alcosystem (n.d)).



Fig. 17. Capsule Endoscopy (Public Domain (n.d)).

Apart from ambulatory and personal medical devices, wireless surgical tracking devices have also been developed to improve the accuracy and efficiency of diagnosis and surgery. Image guidance surgical navigation system uses optical and electromagnetic trackers to track the surgical instruments in the attempt to minimize the human error during surgery. Optical system (Figure 18), uses two infrared cameras to triangulate the position of the target instrument. Figure 19 shows an electromagnetic tracking device developed by Ascension and GE healthcare. The system provides real time feedback of the current position of the biopsy needle, as well as the needle path projection.



Fig. 18. Optical tracking devices for surgical navigation (Metronics).

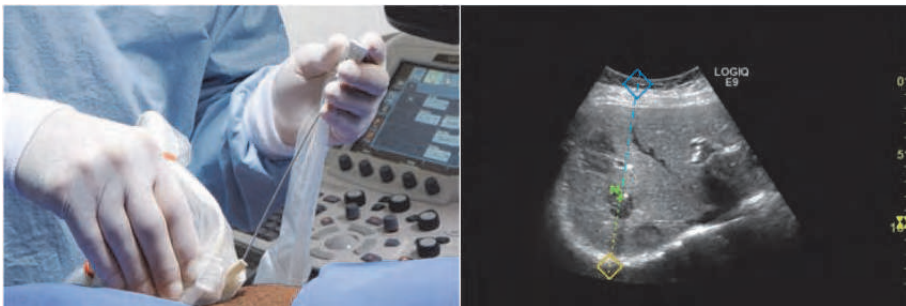


Fig. 19. The biopsy needle is coupled with electromagnetic tracking device to provide feedback of the needle positions (Ascension), (G.E. Healthcare).

## 2.2 Current research

The commercially available devices mentioned in previous section have undergone many years of research and development. The following section is going to look at some of the current researches being done with wireless medical device.

While there are many wireless ambulatory monitoring systems mentioned above, most of them operate in a standalone mode with its own receiver. It would be more beneficial to the physicians and health care professional to centralize all the information into one single device. Tia Gao et al. introduced a wireless sensor network (WSN) system for medical devices. (Gao, et al., 2008) The information from the sensors is wirelessly transmitted to the server, and it can be accessed through handheld devices and computers (Figure 20). The authors tested the system along with medical professions in a mock emergency situation with satisfying results. Another focus of the research is to develop applications from the sensor technologies. Pekka Iso-Ketola et al. developed a wireless medical device using an accelerometer to monitor patient's posture after total hip replacement (THR) surgery (Figure 21). (Iso-Ketola et al., 2008) The devices are also given to the patient such that they can monitor and follow the precautions given by the surgeons.



Fig. 20. Patients' conditions are being monitored through a hand held device (Gao, et al., 2008).

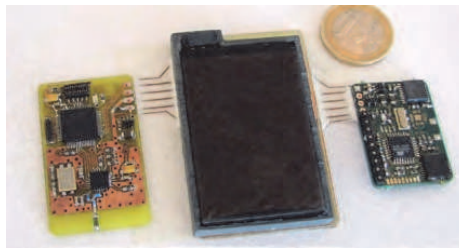


Fig. 21. Wireless hip posture monitoring system (Iso-Ketola, Karinsalo, & Vanhala, 2008).

Shyamal Patel et al. developed a network of wireless acceleration sensing nodes that are attached to different sections of the patient's body as shown in Figure 22 (Patel, et al., 2009). The data collected were analyzed. The calculated parameter can help with the diagnosis of the severity of Parkinson's disease. Stacy Bamberg et al. developed a wireless gait analysis system. A force measuring system is placed within a shoe, and a triaxial accelerometers and gyroscopes attached on the outside of the shoes as shown in Figure 23. (Morris & Paradiso, 2002) The sensors measure the forces and motion on the foot during gait.

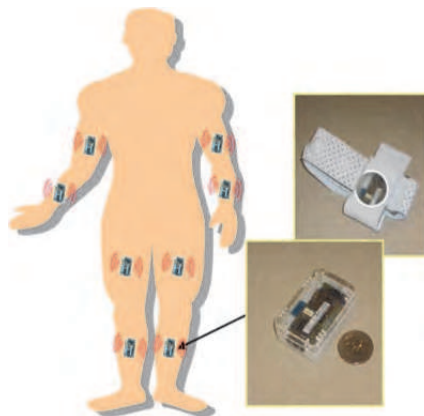


Fig. 22. A network of wireless sensing nodes consists of accelerometers (Patel, et al., 2009).



Fig. 23. Wireless gait analysis system (Morris & Paradiso, 2002).

Aside from the patient monitoring and diagnostic tool, several research groups have been concentrated on implantable medical devices. The technology to design and fabricate micro-electromechanical system (MEMS) sensors and application specific integrated circuit (ASIC) enables embedded measuring systems to be made in an extremely compact fashion. It is now possible to measure *in-vivo* condition that was once impossible. Graichen Friedmar et al. developed a complete embedded system to measure strain within a Humerus implant (Figure 24) (Graichen et al., 2007). Antonius Rohlmann et al. also completed an embedded system to measure the post operative load of spiral implants wirelessly as shown in Figure 25 (Rohlmann et al., 2007). D'Lima and Colwell modified existing knee implants with four load sensors to measure the *in-vivo* stress on the implant after the total knee arthroplasty (Figure 26) (D'Lima et al., 2005). Chun-Hao Chen et al. designed a wireless Bio-MEMS system to measure the C-reactive proteins as shown in Figure 27 (Chen, et al., 2009).

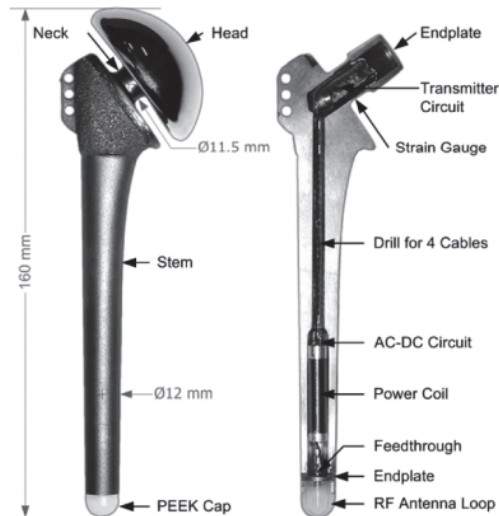


Fig. 24. Telemetry strain measuring Humerus implant (Graichen et al., 2007).



Fig. 25. Wireless load measuring system for vertebral body replacement (Rohlmann et al., 2007)

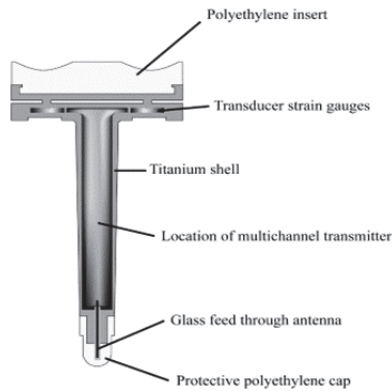


Fig. 26. Telemetry stress measuring knee implants (D'Lima et al., 2005).

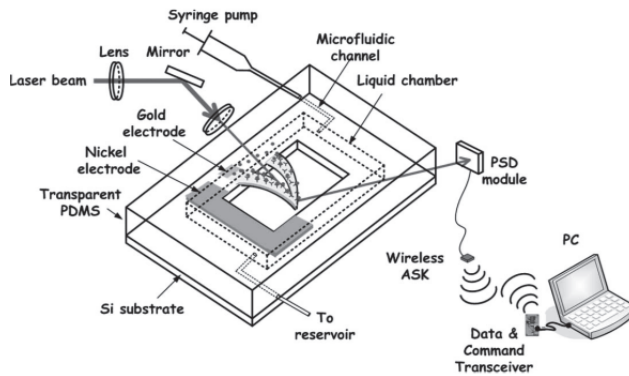


Fig. 27. Wireless Protein detection with BiMEMS (Chen, et al., 2009)

Measuring the forces and contact areas *in vivo* is extremely valuable to researchers, implant designers, clinicians, and patients. Measuring these values post operatively allows for evaluation of the performance of current designs and prediction of future design performance. Data on the *in vivo* load state of joint replacement components is required to understand the structural environment and wear characteristics of that component. Normal loads, load center, contact area, and the rate of loading need to be measured in order to fully understand the kinematics and kinetics of the orthopedic implant. This data can be used to help patients by allowing clinician to monitor implant kinematics, wear, and function. In the cases of predicted premature wear, preventative measures such as orthotics, bracing, or physical therapy could be used to avert the need for revision procedures. Additionally, one of the major postoperative concerns was infection. Currently, there is no effective way to prevent it until symptoms are developed. Biosensing devices that react to disease related protein can monitor and alert physicians to administrate antibiotic during early stage of the infection.

### 3. Wireless signal propagation in hospital environments

The main concern with using wireless tracking and communication technology in the operating room (OR) and other hospital environments is the high level of scatterers and corresponding multipath interference experienced when transmitting wireless signals. While the experiment from Clarke et al. provides quantitative data on how wireless real-time positioning systems perform in the OR, it is also useful to look into narrowband and UWB channels and their effect on narrowband and UWB signals for communication and positioning applications (Clarke & Park, 2006). There are two typical approaches used when modeling wireless channels: the first is statistical models used to model generic environments (e.g. industrial, residential, commercial, etc.), which incorporate LOS or non-line-of-sight (NLOS) measurements taken in the time and frequency domains, which are then used in setting the parameters of these statistical models. The second method uses ray tracing techniques to model specific geometrical layouts (e.g. buildings, cities) and can provide a more accurate depiction of which obstacles and structures will have the greatest effect on wireless propagation. The drawback with ray tracing is the static nature of the results (i.e. results are only valid for a certain scenario of objects placed in the scene). Even if the wireless systems in the operating room are static, other objects will not be including people, patients, the operating table, and medical equipment.

#### 3.1 Channel modelling in the operating room

A useful technique for modeling the operating room channel is to take time domain and frequency domain measurements in the operating room. This can be done both during surgery (live) and not during surgery (non-live) with variable Tx-Rx distances (e.g. 0.5 m to 4 m). Figure 28 and Figure 29 show the time domain and frequency domain setups to collect data in the OR. Figure 30 and Figure 31 show the live and non-live setups where the layout of the dual OR is shown to highlight the Tx and Rx locations for both the live and non-live experiments. Note that both monopole and single element Vivaldi antennas are used for transmission and reception. The basic strategy in the time domain is to send out a narrow UWB pulse, either baseband or modulated by a carrier signal, in the 3.1-10.6 GHz band approved by the FCC. Indoor measurements can also be measured at bands higher than the standard 3.1- 10.6 GHz (e.g. 22-29 GHz) with the understanding that the effective isotropic

radiated power (EIRP) is limited to -51.3 dBm/MHz rather than the -41.3 dBm/MHz available in the lower band (FCC, 2002). Figure 32 shows the experimental setup during the non-live case (Figure 31) for obtaining both time and frequency domain data while Figure 33 shows the experimental setup during an orthopedic surgery. When performing measurements in the frequency domain, the typical approach is to use a vector network analyzer to sweep across the UWB frequency range (e.g. 3.1 – 10.6 GHz) and measure the S-parameter response of the channel where a UWB signal is passed between a transmitting and receiving antenna. The inverse Fourier transform can then be used to convert the signal from a frequency response into an impulse response in the time domain. This allows frequency dependent fading and path loss as well as the RMS delay spread and power delay profile measurements to be obtained. In Figure 29, a vector network analyzer is used to collect data for frequency domain measurements.

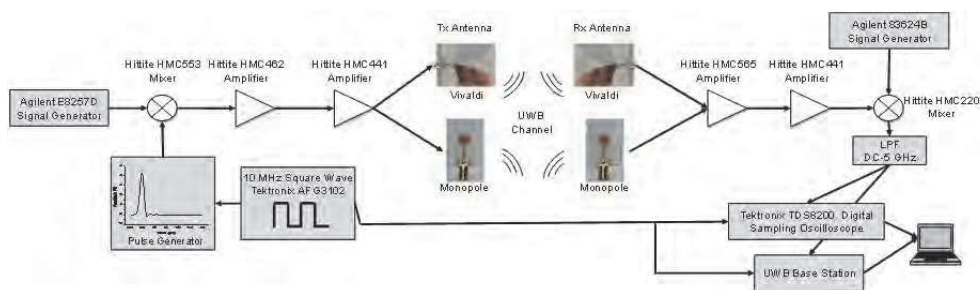


Fig. 28. Experimental setup to collect time domain data in the operating room with the UWB localization system (Mahfouz & Kuhn, 2011).

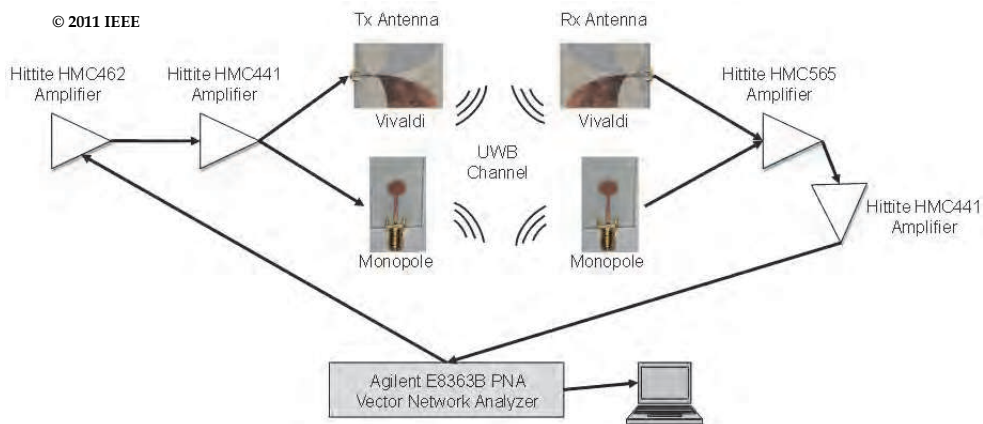


Fig. 29. Experimental setup to collect frequency domain data in the operating room for characterization of the 3.1-10.6 GHz UWB band.

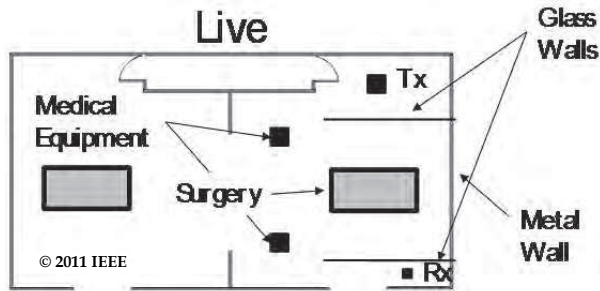


Fig. 30. Layout of dual operating room during surgery outlining the patient table, glass walls, medical equipment, doors, and walls. The Tx and Rx were positioned 4 m apart across the surgery (Mahfouz & Kuhn, 2011).

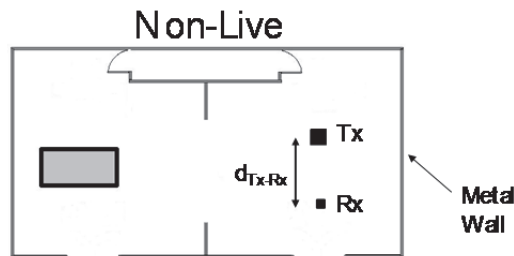


Fig. 31. Layout of dual operating room without surgery taking place where medical equipment, glass walls, and the patient table have been removed. The Tx and Rx were placed in the surgical area and moved from 0.5-4 m apart.

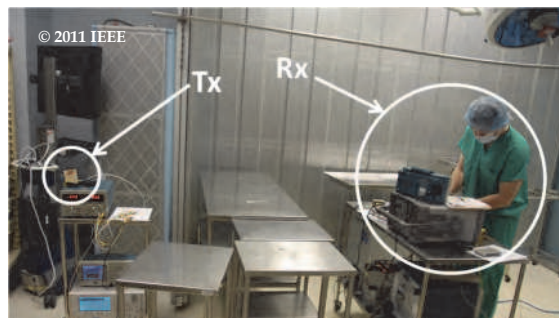


Fig. 32. Experimental setup in the operating room during non-live scenario (Mahfouz & Kuhn, 2011).



Fig. 33. Experimental setup in the operating room during an orthopedic surgery.

### 3.2 Experimental results

Table 4 shows a truncated list of parameters for the LOS operating room environment fit to the IEEE 802.15.4a channel model which were obtained with time domain and frequency domain experimental data. Figure 34 shows the pathloss for the OR environment obtained by fitting experimental data and compared to residential LOS, commercial LOS, and industrial LOS. The pathloss in the OR is most similar to residential LOS, although this can change depending on which instruments are placed near the transmitter and receiver or the locations of the UWB tags and base stations in the room. Figure 35 shows pathloss obtained for a Tx-Rx distance of 0.49 m where the transmitting (monopole) and receiving (Vivaldi) antenna effects have been removed. Small scale fading effects can be seen as well as frequency dependent pathloss, which is captured in the parameter  $\kappa$  in Table 4.

Figure 36 shows an example time domain signal where significant multipath interference is caused by reflections from metal tables and walls. Figure 37 shows an example time domain received signal for a Tx-Rx distance of 1.49 m using the monopole antenna for transmitting and single element Vivaldi antenna for receiving. A decaying exponential is overlaid on the received signal to highlight the intra-cluster decay, defined by  $\gamma_0 = 1.33$  in Table 4. The pathloss of the LOS OR channel is most like a residential LOS environment whereas the power delay profile (PDP) is closer to an industrial LOS environment ( $\gamma_0 = 0.651$ ) where dense clusters of multipath quickly decay (rather than the residential LOS environment where  $\gamma_0 = 12.53$ ). The mean number of clusters ( $\bar{L} = 4$ ) is in between the residential and industrial LOS environments ( $\bar{L} = 3$  and  $\bar{L} = 4.75$ ). The inter-cluster decay constant and inter-cluster arrival rate ( $\Lambda$  and  $\Gamma$ ) for the operating room channel are more similar to the industrial LOS channel rather than the commercial or residential LOS channels. The operating room LOS channel is similar to the industrial LOS channel in its time domain characteristics (i.e. multipath interference and decay) while it is similar to the residential LOS channel in its frequency domain characteristics.

| Operating Room   | LOS   |
|------------------|-------|
| $PL_0$ [dB]      | -47.5 |
| $n$              | 1.33  |
| $\kappa$         | 0.95  |
| $\bar{L}$        | 4     |
| $\Lambda$ [1/ns] | 0.095 |
| $\lambda$ [1/ns] | n/a   |
| $\gamma_0$ [ns]  | 1.33  |
| $k_\gamma$       | 0.217 |
| $\Gamma$ [ns]    | 10.8  |

Table 4. Summary of parameters fit to IEEE 802.15.4a channel model with experimental UWB data taken in the operating room (Mahfouz et al., 2009).

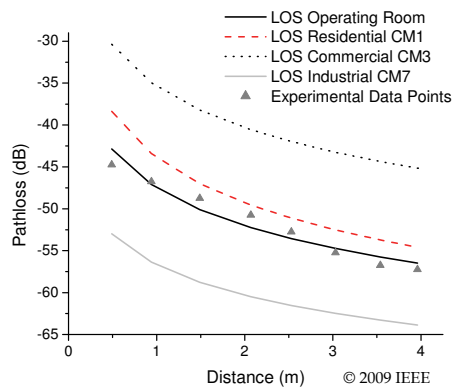


Fig. 34. Comparison of pathloss for IEEE 802.15.4a LOS channels. The pathloss for the OR environment is most similar to residential LOS (Mahfouz et al., 2009).

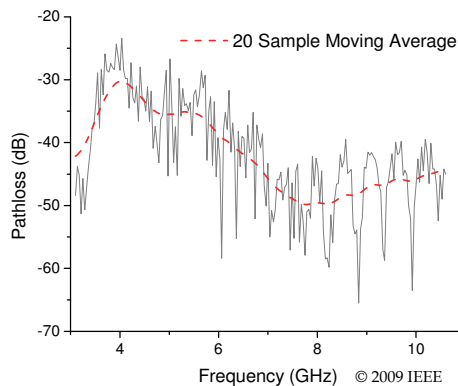


Fig. 35. Pathloss obtained with the Tx and Rx placed 0.49 m apart where effects from the transmitting (monopole) and receiving (Vivaldi) antennas have been removed. The frequency dependence,  $\kappa$ , can clearly be seen as well as small scale fading effects (Mahfouz et al., 2009).

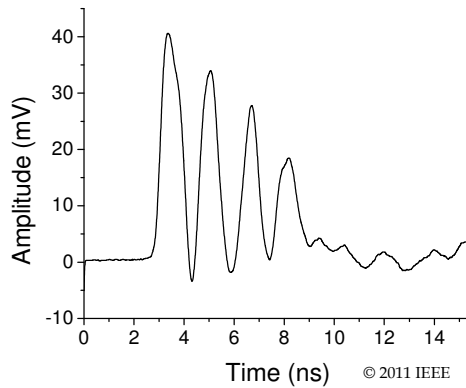


Fig. 36. Experimental received time domain signal with noticeable multipath interference caused by metal tables and walls in the operating room (Mahfouz & Kuhn, 2011).

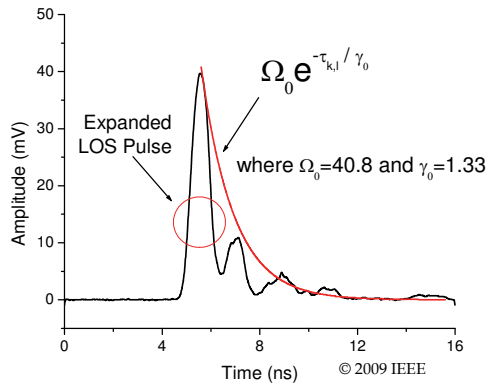


Fig. 37. Example received signal in the time domain for a Tx-Rx distance of 1.49 m highlighting the distortion (seen as expansion) in the LOS pulse due to a dense cluster of multipath rays. The overlaid exponential is fit using  $\gamma_0$  as outlined in Table 4 to show the intra-cluster decay of the LOS cluster (Mahfouz et al., 2009).

### 3.3 Electromagnetic interference in the operating room

Electromagnetic interference (EMI) in the OR was measured across a wide frequency range in the context of comparing the interference present in useable frequency bands for narrowband and UWB communication and localization systems (for available bands see Table 3).

#### 3.3.1 OR indoor environment

EMI was measured over a large frequency band (200 MHz – 26 GHz) in the OR during four separate orthopedic surgeries. Figure 38 shows the experimental setup in the OR. Besides the operating table, numerous other pieces of medical equipment were present during the surgery including an anesthesia machine, ventilator, surgical lamps, various monitoring

equipment, visualization screens, carts containing necessary orthopedic surgical tools, drills, etc. Also, numerous people were present including the surgical team, orthopedic company representatives, and spectators observing the surgery. The combination of people and medical equipment closely packed into the OR creates a dense multipath indoor environment that can greatly disrupt standard RFID tracking systems. UWB systems have inherent advantages that make them a strong candidate for use in dense multipath environments such as the OR.

### 3.3.1 Experimental setup

Various hardware was needed to get accurate measurements across the wide band of 200 MHz – 26 GHz. It should be noted that all reported gain and noise figure values are averages across the frequency range of operation. Figure 39 shows the four antennas used to cover the entire frequency range. The standard setup for each of the frequency bands measured included an antenna, two stages of amplification, and a spectrum analyzer for visualization. Commercial off-the-shelf components were used whenever possible. Table 3 lists the major medical, scientific, and UWB frequency bands in the US and Europe. A majority of the scientific and medical bands in both Europe and the US fall between the frequencies of 200 MHz – 3 GHz. Also, most RFID systems operate in the MHz range up to 3 GHz. Even though RFID systems can operate at 5.8 GHz or 24.125 GHz, limitations still exist on how well a system with small bandwidth can handle the dense multipath environment of the OR at these high frequencies. When looking at different wireless bands currently in use, whether WLAN, cellular phones, GPS, or medical, the advantages of operating in the higher frequency bands of 3.1 – 10.6 GHz and 22 – 29 GHz useable for UWB become clear.



Fig. 38. Experimental setup in the OR.

### 3.3.2 Experimental results

Electromagnetic interference was measured over the frequency range of 200 MHz – 26 GHz. The results from these measurements can be seen in Figure 40–42. A number of signals were detected in the lower frequency range of 400 MHz – 2.5 GHz. As shown in Figure 40, no appreciable signals were picked up between 200 – 800 MHz. Although there is a small spike near 470 MHz, it is only 6dB above the noise floor and is considered noise. Also, there are no licensed frequency bands in the US that could correspond to the 470 MHz peak. Figure 41 shows the frequency band from 800 MHz – 3 GHz. A number of different signals were

found in this frequency range. The two strongest signals, which were found at 872 MHz and 928 MHz, correspond to CDMA2000 uplinks and downlinks. The peak at 1.95 GHz also corresponds to a US cellular band. Finally, the peak at 2.4 GHz is caused by WLAN and Bluetooth components. Figure 42 shows the frequency band from 3 – 26 GHz. No noticeable signals were picked up across this entire band. This is somewhat unexpected since there are ISM and WLAN bands between 5 – 6 GHz, which could be the major culprit causing interference that could affect UWB systems.

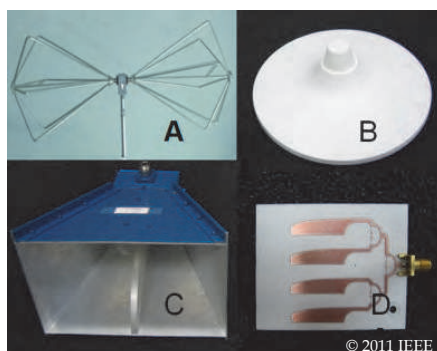


Fig. 39. Antennas used in OR measurements: a) biconical, b) multiband disc, c) broadband TEM horn, d) 4-element Vivaldi array (Mahfouz & Kuhn, 2011).

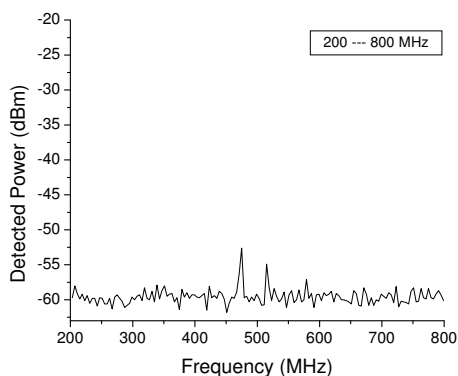


Fig. 40. Measured EMI over frequency range of 200 – 800 MHz (Mahfouz & Kuhn, 2011).

The frequency bands containing noticeable EMI correspond to widespread technologies that will likely be seen in the average OR. One surprise was the almost complete absence of US scientific and medical bands. Many medical devices do conduct wireless operations at the frequency bands summarized in Table 3, but besides the WLAN signal at 2.4 GHz seen in Figure 41, no significant EMI corresponding to these frequency bands was detected in the OR. As outlined in Table 3, there is another UWB frequency band from 22 – 29 GHz that can be used for localization systems. As seen from Figure 42, there is no EMI in the band from 22 – 26 GHz. One reason for having no EMI is that very few licensed bands exist between 22 – 29 GHz that would affect an OR. Also, signals in this frequency band tend to be attenuated

more by the atmosphere and are typically used for short range applications. Using UWB for localization in the OR holds a distinct advantage over other technologies because of both the large bandwidth used as well as the higher frequencies available for operation.

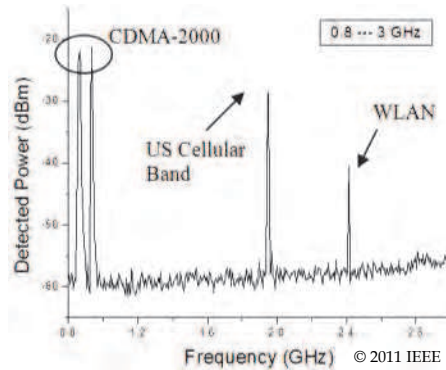


Fig. 41. Measured EMI over frequency range of 800 MHz - 3 GHz (Mahfouz & Kuhn, 2011).

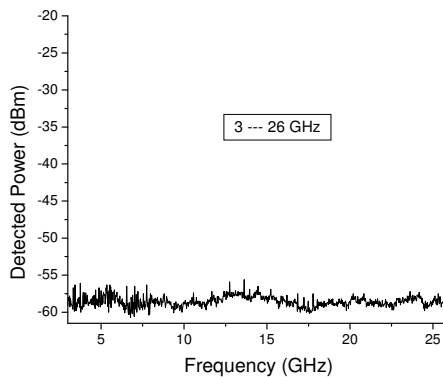


Fig. 42. Measured EMI over frequency range of 3 - 26 GHz.

#### 4. High accuracy positioning systems for indoor environment

Although UWB positioning systems are well established in their use for indoor applications requiring 3-D real-time accuracy on the level of 10-15 cm, current commercial systems have not been able to meet the stringent accuracy specifications (e.g. 1-2 mm or sub-mm 3-D) of the next level of applications including smart medical instruments, surgical navigation, and tracking in wireless body-area-networks.

##### 4.1 Development of a high accuracy ultra-wideband positioning system

The challenges in developing a millimeter range accuracy real-time non-coherent UWB positioning system include: generating ultra-wideband pulses, pulse dispersion due to antennas, modeling of complex propagation channels with severe multipath effects, need for extremely high sampling rates for digital processing, noise and sensitivity of the UWB

receiver, local oscillator phase noise (in the case of a carrier-based system), antenna phase center variation, time scaling, jitter, and degradation due to overall system calibration. For such a high precision system with mm or even sub-mm accuracy, all these effects should be accounted for and minimized. The complete setup of the non-coherent UWB positioning system is shown in Figure 43. The source of the non-coherent UWB positioning system is a step-recovery diode (SRD) based pulse generator with a pulse width of 300 ps and bandwidth of greater than 3 GHz. The Gaussian pulse is up-converted with an 8 GHz carrier and then transmitted through an omni-directional monopole UWB antenna. Multiple base stations are located at distinct positions to receive the modulated pulse signal. The received modulated Gaussian pulse at each base station first goes through a directional Vivaldi receiving antenna and then is amplified through a low noise amplifier (LNA) and demodulated to obtain the I signal. Only one channel rather than I/Q is required since energy detection and carrier offsets are also applied at the UWB receiver. After going through a low pass filter (LPF), the I channel is sub-sampled using an UWB sub-sampling mixer, extending the signal to a larger time scale while maintaining the same pulse shape (Zhang et al., 2007). The PRF clocks are set to be 10 MHz with an offset frequency of 1-2 kHz between the tag and base stations which corresponds to an equivalent sampling rate of 50-100 GS/s. Finally, the extended I channel is processed by a conventional analog to digital converter (ADC) and standard FPGA unit. Leading-edge detection is performed on the FPGA. The time sample indices are sent to a computer where additional filtering and the final time-difference-of-arrival (TDOA) steps are performed to localize the 3-D position of the UWB tag.

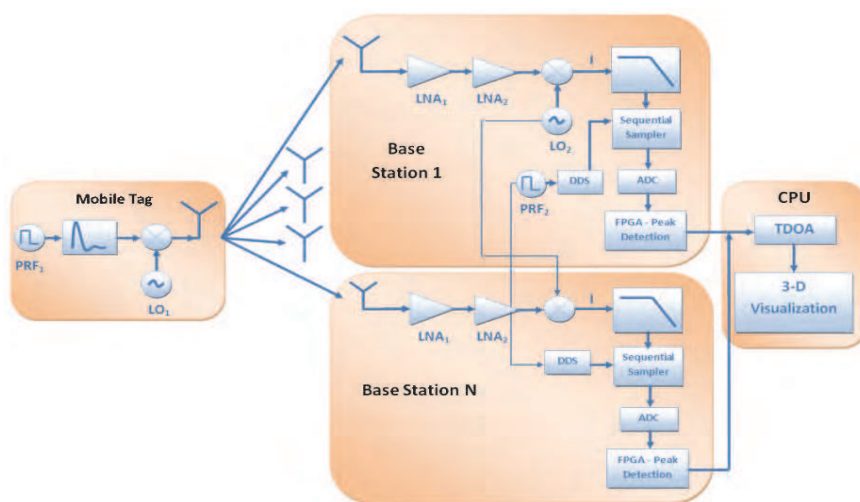


Fig. 43. System architecture of non-coherent UWB positioning system which includes a carrier-based transmitted signal at the tag and a combination of downconversion and energy detection at the UWB receiver.

To detect narrow pulses on the order of a few hundred picoseconds (i.e. 300 ps or 3 GHz bandwidth in our system), analog to digital converters with at least 6 GS/s are needed to satisfy the Nyquist criterion. However, such high performance ADC units are currently

either not commercially available or too expensive for most applications. A realistic alternative approach to real-time sampling is to sub-sample the UWB pulses while maintaining the initial pulse shape through extended time techniques. The extended UWB signals can then be handled by readily available commercial ADCs, reducing overall system cost (Zhang et al., 2007). The sampler utilizes a simple broadband balun structure and a balanced topology.

The non-coherent architecture of the current UWB positioning system places stringent requirements on phase noise specifications of the local oscillators at the transmitter and receiver. The use of a reference tag partially mitigates the local oscillator phase noise and temperature effects at the UWB receivers. Even with a reference tag, the phase noise presents a formidable challenge to achieving millimeter 3-D real-time accuracy. High phase noise carriers (e.g. free running voltage controlled oscillators) cause up to an order of magnitude (e.g. cm) greater error than low phase noise carriers. When attempting to achieve millimeter and sub-mm accuracy, phase center variation of the antennas at the Tx/Rx is an important source of error which needs to be taken into account. The transmitter employs a UWB monopole antenna which provides an omni-directional radiation pattern with minimal phase center variation while the receiver utilizes a single element Vivaldi antenna for a radiation pattern directed at the view volume of interest. Noticeable variation of the phase center is observed in both the E and H cuts especially for angles greater than  $\pm 30^\circ$ . High accuracy positioning systems must employ calibration techniques to remove the phase center effects. For example, antennas used for GPS systems go through an advanced automated calibration process which uses high precision robots to move the antennas to 6000-8000 distinct points in calibrating out phase center effects. More challenges appear in achieving high accuracy real-time indoor positioning at the system-level. Cable length effects at the UWB receivers must be accounted for and statically calibrated and removed from the system. Time scaling effects due to system clock drift must be characterized and calibrated out of the final TDOA calculations in a dynamic manner when moving around the view volume. Time scaling effects change across the view volume due to the differences in LOS ranges  $r_i$  between the tag and each base station. The 3-D variation must be calibrated out in order to get a highly accurate indoor positioning system achieving stable millimeter range accuracy. Future improvements for this UWB indoor positioning system include the addition of real-time, multi-tag access (Kuhn et al., 2011) and utilizing comprehensive simulation frameworks for accurate simulation of advanced mixed signal systems in realistic indoor environments (Kuhn et al., 2010).

## 4.2 Real-time experimental results

Two 3-D experiments with unsynchronized LOs and PRF clock sources were carried out, where a minimum of four base stations are needed for the 3-D measurements.

### 4.2.1 3-D dynamic free motion

Figure 44 shows a four base station setup where the 3-D positions were measured for each base station utilizing the Optotrak 3020 system, which also serves as a reference for comparing the 3-D real-time accuracy of our UWB localization system. The Optotrak 3020 has 3-D real-time accuracy of better than 0.3 mm. It should be noted that the spatial spread of the base stations along the z-axis is the largest (2498 mm), while the x-axis is the smallest

(1375 mm). In the dynamic mode, the tag is moving randomly inside the 3-D space as shown in Figure 44. The 3-D motion of the tag is then plotted and UWB measurements are compared with Optotrak measurements. RMSE is used to report the error since it is the true unbiased error when data values fluctuate above and below zero. Figure 45 plots the UWB trace and Optotrak trace in the 3-D dynamic mode.

Figure 46 shows the 3-D dynamic errors in the  $x$ ,  $y$ , and  $z$  axes over 1000 measured points. The overall 3-D RMSE is 6.37 mm. The error along the  $x$ -axis contributed most to the overall distance error, which can be explained by the limited spatial spread of base stations along the  $x$ -axis and can be calculated using the PDOP definitions in (Mahfouz et al., 2008). Such error can be mitigated through better arrangement of the base stations along the  $x$ -axis.

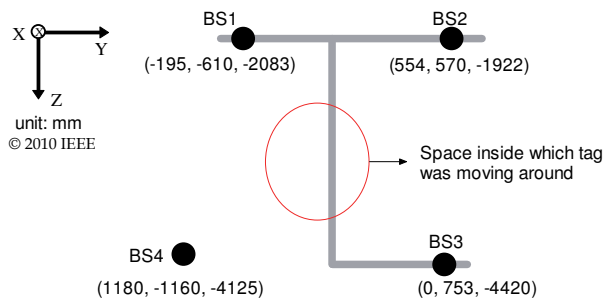


Fig. 44. 3-D unsynchronized localization experiments, 4 base station distribution with locations for each base station (Zhang et al., 2010).

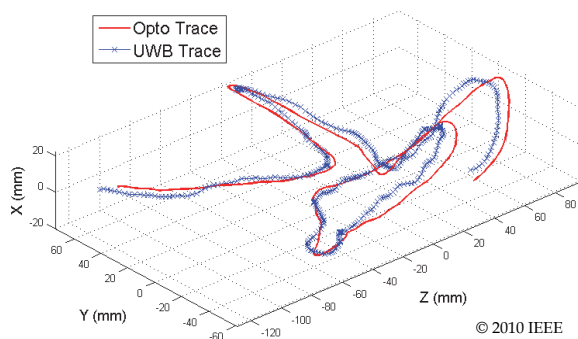


Fig. 45. 3-D dynamic random mode with energy detection. UWB trace is compared to Optotrak trace (Zhang et al., 2010).

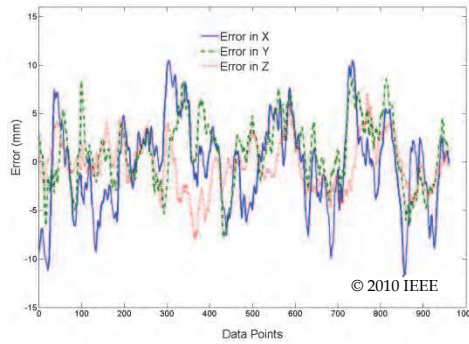


Fig. 46. 3-D dynamic mode with energy detection.  $x$ ,  $y$  and  $z$  axes error compared to Optotrak measurements (Zhang et al., 2010).

#### 4.2.2 3-D robot tracking

The next non-coherent 3-D experiment is to dynamically track the robot position. The monopole antenna and the reference Optotrak probe are tied together and fixed to the arm of the CRS A465 robot. The robot arm set up is shown in Figure 47. Finally, the base stations can be seen in Figure 48. The robot was pre-programmed to specifically cover 20 distinct static positions in a 3-D volume, stopping for three seconds at each position and then moving to the next position and so on. The measured traces by the UWB system are compared to the Optotrak reference system as shown in Figure 49. Figure 50 shows the 20 distinct static positions taken by both the UWB and the Optotrak systems. The overall dynamic 3-D robot tracking RMSE is 5.24 mm. In Table 5 the real-time non-coherent 3-D experimental results are summarized under various scenarios. The reported RMSE are based on 1000 continuous data points recorded and compared to the Optotrak 3020 system, which served as the real-time reference of our UWB localization system and provides a 3-D accuracy of better than 0.3 mm.

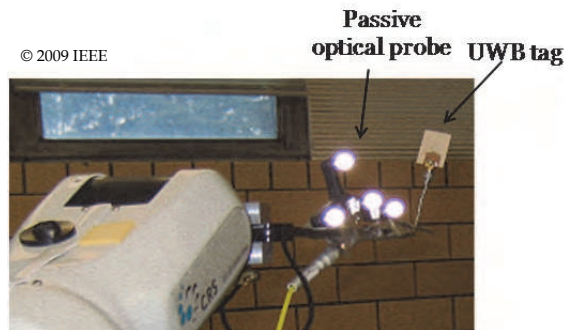


Fig. 47. Robot arm with UWB monopole and optical tracker attached (Mahfouz et al., 2009).



Fig. 48. Experimental setup outlining base station positions.

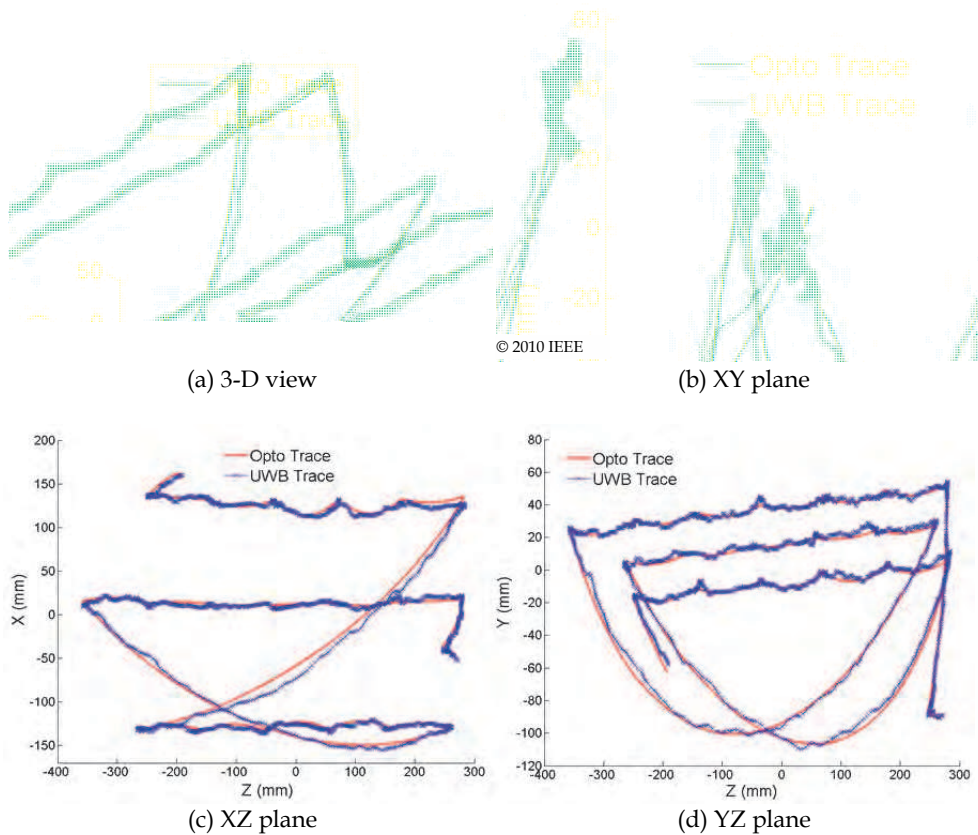


Fig. 49. 3-D dynamic robot tracking. UWB trace compared to Optotrak trace: (a) 3-D view; (b) XY plane; (c) XZ plane; (d) YZ plane (Zhang et al., 2010).

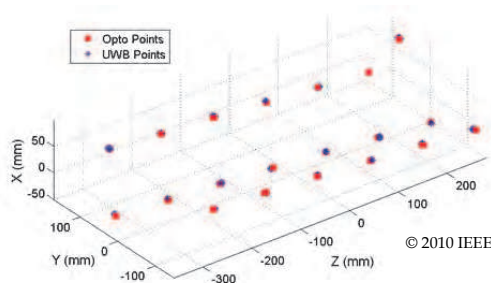


Fig. 50. 3-D robot tracking at static positions. UWB points compared to Optotrak points (Zhang et al. 2010).

| 3-D Experiments                                | RMSE (mm) |
|--|-----------|
| Tag free random motion                         | 6.37      |
| Robot dynamic tracking                         | 5.24      |
| Robot static positions (20 distinct locations) | 4.67      |
| Static position w/ 106 times of average        | 1.98      |

Table 5. Error Summary – 3-D unsynchronized localization experiments (Zhang et al. 2010).

## 5. Wireless MEMS sensors used as feedback control in an orthopedic surgical navigation system

Over the past decade, orthopedic companies have been trying different methods and protocols to eliminate one of the primary causes of implant failure in total knee arthroplasty (TKA), which is the malalignment of the implants to the biomechanical axis of the patient. To properly place the implant, the gaps after the resections between the femur and tibia during extension and 90 degrees flexion have to be parallel to each other and the gap size have to be the same (Figure 51). However, the surgeons are usually working with a small incision with limited access to the joint. Moreover, the knee joint are stabilized by the medial and lateral collateral ligaments. The laxity of the ligaments can affect the gap balance.

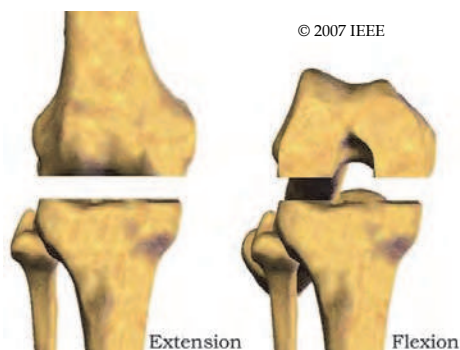


Fig. 51. Flexion and Extension gap between the femur and tibia (To, 2007)

In order to help the surgeons to assess the tightness of the joint after resection, an instrument was designed to provide quantitative feedback to the users. A wireless strain measuring device was designed. The high level system design is shown in Figure 52. Two types of sensors were investigated in the design of this instrument. The first type of sensor is piezo-resistive based microcantilever as shown in Figure 53. When a piezo-resistive element undergoes stress, the resulting strain causes changes in the resistance of the material. Hence, it is possible to use to measure strain by monitoring the resistance of the material.

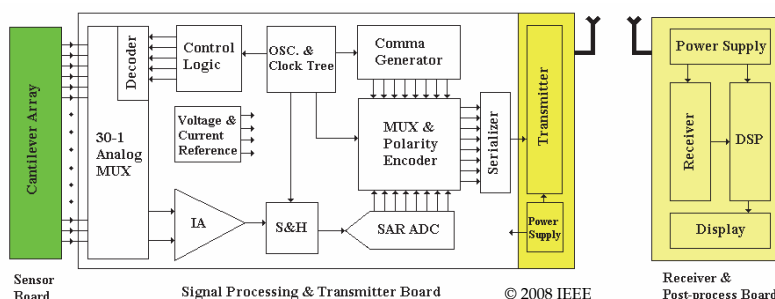


Fig. 52. High level design of a wireless strain measuring system (Qu et al., 2008)

The piezo-resistive microcantilevers here are used to measure a macro pressure that causes a deflection in the microcantilever beam. The microcantilevers are tiny and extremely fragile. In addition, silicon is not a FDA-approved biocompatible material unless specifically doped. This specific application to measure macro forces requires a protective layer with a material that damps the applied stress and provides a biocompatible interface for bodily contact. Medical grade epoxy was used as a protective material for the sensors as well as providing a biocompatible surface to interface with the soft tissues. The epoxy was cured over the microcantilevers to protect and to give a desirable force readout range. Curing procedures and epoxy homogeneity were investigated to create the most reliable, non-interfering encapsulation. Parameters investigated included viscosity, cure time, working time, heat cure, and minimization of bubbles and microbubbles. EP30MED (Masterbond, Inc.) was chosen as the most favorable epoxy for encapsulation. A microcantilever that was encapsulated with a 2mm thick epoxy was used for mechanical testing as shown in Figure 54. An Instron 5544 testing machine was used. The properties of the encapsulated sensor are shown in Table 6.

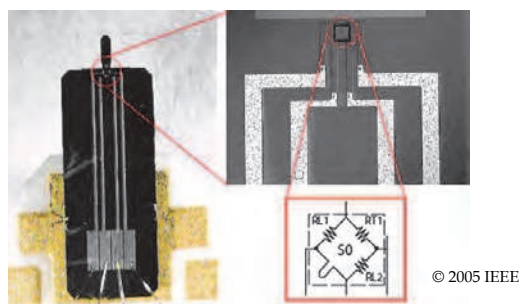


Fig. 53. Piezo resistive microcantilever (Nascatec, Stuttgart, Germany) [To & Mahfouz, 2005]

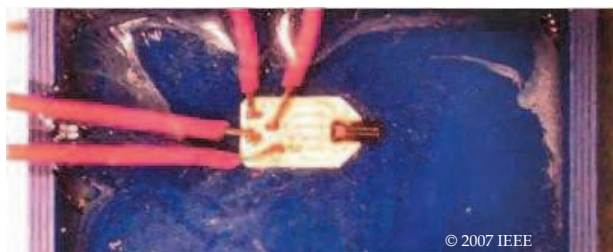


Fig. 54. Microcantilever encapsulated in EP30MED epoxy.

| Parameter     | Value                      |
|---------------|----------------------------|
| Range         | 0 – 300 kPa                |
| Input         | 0 – 3.3V +/- 1%            |
| Linearity     | 0.625mV/kPa (over range)   |
| Repeatability | 0.6444mV/kPa (over range)  |
| Sensitivity   | 0.35455mV/kPa (over range) |

Table 6. Properties of microcantilever encapsulated in 2mm of EP30MED (Qu et al., 2010)

The readout circuit for the microcantilever system was tested with off-the-shelf components using an MSP430 (Texas Instrument) as microcontroller, ADG726 (Analog Device) as multiplexer, INA331A2 (Texas instrument) as instrumental amplifier, and MAX1472/1473 as transmitter and receiver. The readout circuit is too bulky to be fitted inside a surgical instrument. As a result, an application specific integrated circuit (ASIC) is designed specifically for the reading of the microcantilever sensors. The ASIC includes the multiplexer, signal conditioning circuit, analog to digital converter (ADC), and a buffer interfacing with the transmitter. The footprint of the ASIC is shown in Figure 55. The specification of the ASIC is shown in Table 7. The gain of the amplifier can be adjusted via an external resistor. After examining the outputs of the microcantilever, the gain was configured to 72. The overall system RSS error with microcantilever embedded within 2mm thick of EP30MED is approximately +/- 1.79kPa.



Fig. 55. ASIC designed for microcantilever readout (Left: ASIC footprint, Right: ASIC with testing package) (Qu et al., 2010)

| Parameters                     | Values                  |
|--------------------------------|-------------------------|
| Analog input channels          | 16                      |
| Analog MUX switching frequency | Oscillator dependent    |
| A/D Converter input range      | ~ 200mV - 1589mV        |
| A/D Converter resolution       | 8bit                    |
| A/D Converter rate             | 772 kHz                 |
| Band gap reference             | 1.249V                  |
| INA gain                       | Gain resistor dependent |
| INA phase margin               | 65°                     |
| INA Unit gain bandwidth        | ~ 2.4 GHz               |
| A/D ENOB                       | 7.24 bit                |
| A/D SNDR                       | 45.4 dB                 |
| A/D SFDR                       | 56.4 dB                 |
| DNL                            | +0.57/-0.42 LSB         |
| INL                            | +1.3/-0.2 LSB           |
| Power supply                   | 2.6 - 4.4V              |

Table 7. ASIC specification (Qu et al., 2010)

The final design of the instrument is designed to fit within a spacer block (Figure 56). The spacer block is placed within the resection gap to identify the tightness of the joint. Moreover, identifying the location of the high strain area can help the surgeons in balancing the joint with appropriate ligaments release. The system design is separated into 3 layers. An array of 30 microcantilever are arranged and wirebonded onto the circuit board. The bottom most circuit board is the ASIC and the battery layer as shown in Figure 57. Two switches are used to connect the poly Li<sup>+</sup> batteries to the electronics and sensors. Traditional coin cell batteries are not suitable for this design as they are too large in size and they are incapable of powering all 30 microcantilevers, which is about 70mA. The poly Li<sup>+</sup> batteries can be made in customizable shape and they are rechargeable. For the prototype, a USB socket is used to recharge the batteries. High density sockets are used to connect the ASIC layer to the sensors layer.

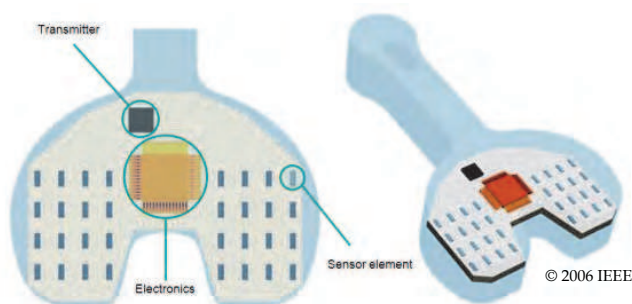


Fig. 56. Instrumented Spacer Block [To et al., 2006].

The middle layer is the TX PCB. The transmitter is using MAX1473 and configured the carrier frequency to 433MHz. The material for the circuit board was changed to 0.0020" rogers 4350 for better performance. A chipped antenna is used to further reduce the volume

required from traditional whipped antenna. The assembled PCB is shown in Figure 57. Each side of the PCBs has 15 active sensing microcantilevers and 1 additional microcantilever for reference on the left side of the PCB.

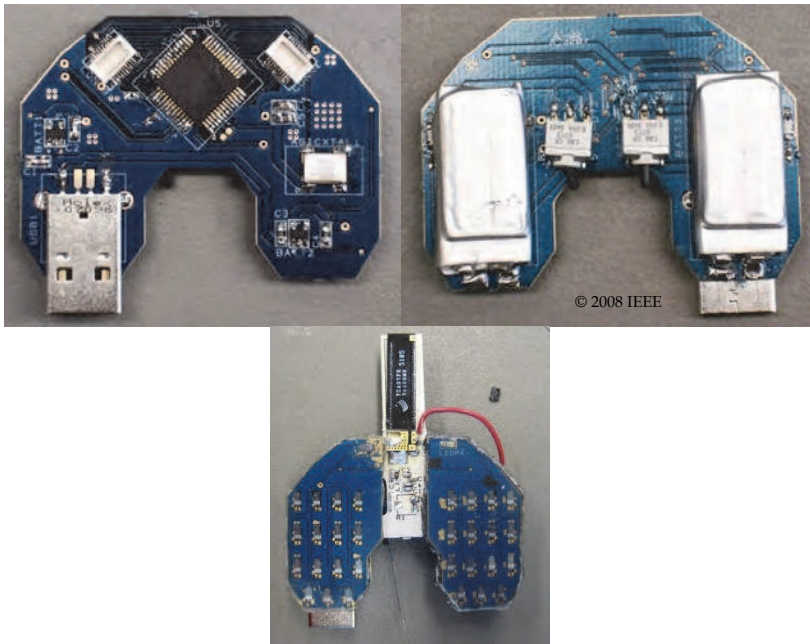


Fig. 57. Left: Top view of the signal processing layer; Center: Bottom view showing the batteries; Right: Top view of assembled PCB (Right) with 15 microcantilevers arrayed on each condyle. (Qu et al., 2008)

The second type of sensor being investigated was capacitive based MEMS device. Strain sensing is accomplished by embedding pairs of electrodes with specific geometries in a biocompatible material. Deformation of the embedding materials causes changes in the configuration of the capacitor electrodes. However fabricating MEMS devices on polymeric materials is not as straight forward as with silicon substrate. Researchers have shown that polyimide can be used as a substrate material, and parylene can be used as the dielectric material (1.5  $\mu\text{m}$ ). It is noted that parylene has served as a substrate layer in early capacitive fabrication when the sensor was left on the silicon wafer, but it poses a problem due to adhesion and mechanical strength of the thin film during removal from the silicon substrate. A negative-resist based photolithography fabrication was implemented to reduce time and number of steps for fabrication. The electrodes consist of a 10 nanometer (nm) titanium adhesion layer and 300 nm of gold deposited on the substrate via physical vapor deposition. Array design is multi-faceted to understand the behavior of the sensors at a small scale and to optimize design to boost readout speed, increase nominal capacitance, and decrease crosstalk and parasitic effects specific to the configuration of this array. Increasing nominal capacitance is most easily achieved through larger electrode size and thinner dielectric layers, thus presenting a tradeoff between keeping sensor size to a minimum and nominal

capacitance at an appropriate level for accurate measurement. Similarly, the spacing needs to be optimized between closeness (providing high spatial resolution across the array), and crosstalk (sensors too close to one another affecting readout). A uniaxial and triaxial strain measuring device was fabricated as shown in Figure 58.

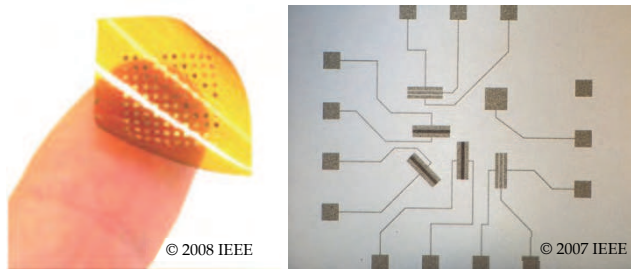


Fig. 58. Capacitive based MEMS strain measuring device (Left: Uniaxial(Pritchard et al., 2008), Right: Triaxial (Evans III, 2007)).

An array of sensors was tested using an MTS (Eden Prairie, MN) 858 Table Top System mechanical testing machine with a 2.5 kN load cell. The load profile is shown in Figure 59. A protective polyimide layer was placed over the electrodes and a second protective layer over the entire assembly. Unlike the microcantilever sensors, no protective epoxy layer was required. Similar to the piezoresistive microcantilever, a transition was made from using off-the-shelf IC to ASIC electronics for the capacitive MEMS sensors. An ASIC consisting of diode array, matched capacitor capacitance to voltage converter and a custom designed instrumental amplifier as shown in Figure 60.

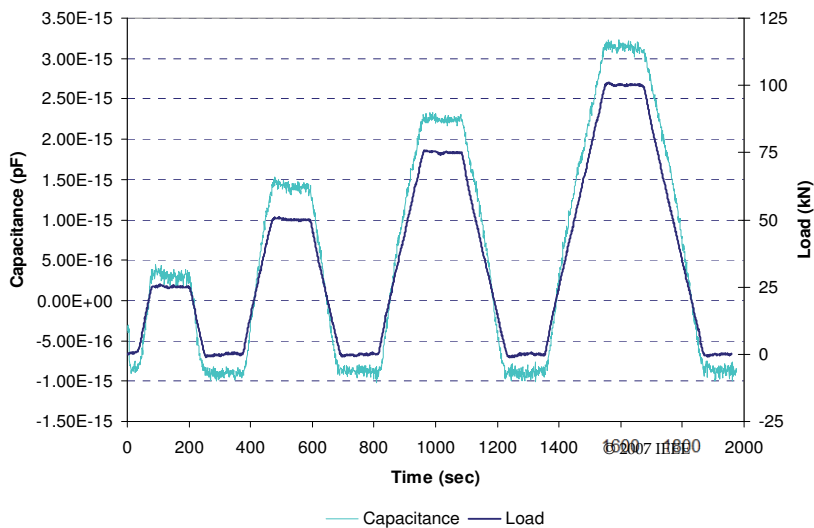


Fig. 59. Load profile for capacitance array test. Test is from 5 pF capacitor array (Evans III, 2007).

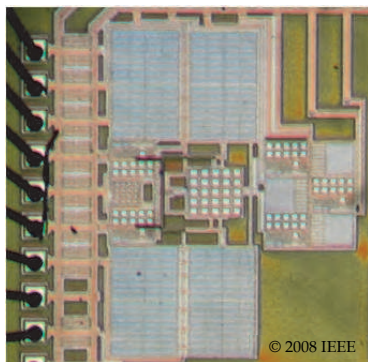


Fig. 60. Microscopic view of ASIC after fabrication (Haider et al., 2008)

The capacitive MEMS sensors can be fabricated at high density such that hundreds of sensors can be placed within the same area as the microcantilever system. Addressing and processing these sensors, as well as transmitting these data at a high speed manner are some of the major challenges in this system.

## 6. Conclusion

Wireless medical devices can greatly improve efficiency and productivity for the healthcare sector. Current wireless technologies enable compact design and are inexpensive to manufacture. With the increasing amount of personal information being monitored and transmitted wirelessly, security measures are one future trend in wireless technology research. Protecting patient privacy is a vital aspect in remote patient monitoring systems.

Despite the increasing number of commercial wireless medical products, many of them use different wireless protocols, and data are transferred at various data rates. Hence, one of the focuses will be increasing the degree of integration for wireless medical healthcare monitoring systems. There will also be an increasing use of implantable and ingestible wireless medical devices, as it provides means to access and gather data and information that were previously impossible.

As research advances, there will be a demand for higher resolution to improve the accuracy of indoor wireless positioning systems. Highly accurate wireless positioning has many applications in medicine including computer assisted surgery, smart surgical instruments, and accurately locating sensors in body area networks. As the amount of integration and the complexity of the system increases, the current wireless protocols will not be sufficient to provide a large enough bandwidth for real time applications. Thus, high speed, high data rate design and protocols will be needed in future wireless technologies.

While it is important to research and develop more advanced wireless medical devices, it is also important to focus on application development for these devices. The ultimate goal for biomedical devices is to provide tools to assist the physicians, and to improve the quality of life of the patients. Application development plays a crucial role in developing these instruments. It is also worth mentioning that some of the devices measured in this article are very similar to each other, in which they share the same basic components. However, they are fine tuned to be used in different applications, and this is critical in developing a device robust enough to meet the stringent requirements of the medical field.

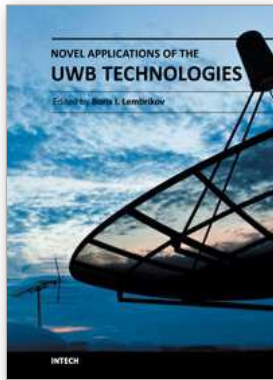
## 7. Reference

- Alavi, B., & Pahlavan, K. (2006). Modeling of the TOA-based distance measurement error using UWB indoor radio measurements. *IEEE Comm. Let.*, 10 (4), 275-277.
- Alcosystem (n.d.). Retrieved from [http://www.alcosystems.se/iBAC\\_1sidig.pdf](http://www.alcosystems.se/iBAC_1sidig.pdf)
- Ascension (n.d.). Retrieved from <http://www.ascension-tech.com>
- Chen, C.-H., Hwang, R.-Z., Huang, L.-S., Lin, S.-M., Chen, H.-C., Yang, Y.-C., et al. (2009). A Wireless Bio-MEMS Sensor for C-Reactive Protein Detection Based on Nanomechanics. *IEEE Transactions on Biomedical Engineering*, 56(2), 462-470.
- Clarke, D., & Park, A. (2006). Active-RFID system accuracy and its implications for clinical applications. *IEEE Symp. on Computer-Based Med. Sys.* (pp. 21-26). Salt Lake City, USA.
- Lifescience Corp, L. (n.d.). Retrieved from <http://www.lifescynccorp.com/products/wireless-system.html>
- D'Lima, D., Townsend, C., Arms, S., Morris, B., & CW, C. (2005). An implantable telemetry device to measure intra-articular tibial forces. *Journal of Biomechanics*, 38, 299-304.
- Ekahau Real-Time Location System Brochure. (2008). (Ekahau, Inc) Retrieved from [http://www.ekahau.com/images/stories/documents/ekahau\\_rtls\\_brochure\\_en\\_122007\\_lo.pdf](http://www.ekahau.com/images/stories/documents/ekahau_rtls_brochure_en_122007_lo.pdf)
- Ellinger, F., Eickhoff, R., Gierlich, R., & Hüttner, J. (2007). Local positioning for wireless sensor networks. *IEEE Globecom Workshops*, (pp. 1-6). Washington DC, USA.
- Emotiv. (n.d.). Retrieved from <http://www.emotiv.com>
- Evans III, B. M. (2007). *MEMS Capacitive Strain Sensing Elements for Integrated Total Knee Arthroplasty Prosthesis Monitoring*. Knoxville, TN, USA: University of Tennessee.
- Falsi, C., Dardari, D., Mucchi, L., & Win, M. (2006). Time of arrival estimation for UWB localizers in realistic environments. *EURASIP Journal on Applied Signal Processing*.
- FCC. (2002). The first report and order regarding ultra-wideband transmission systems. *FCC 02-48, ET Docket*, 98-153.
- Feger, R., Wagner, C., Schuster, S., Jager, H., & Stelzer, A. (2009). 77-GHz FMCW MIMO radar based on an SiGe single-chip transceiver. *IEEE Trans. Microwave Theory and Tech*, 57 (5), 1020-2035.
- Fontana, R. (2004). Recent system applications of short-pulse ultra-wideband (UWB) technology. *IEEE Trans. Microwave Theory and Tech*, 52 (9), 2087-2104.
- Fujii, A., Sekiguchi, H., Asai, M., Kurashima, S., Ochiai, H., & Kohno, R. (2007). Impulse radio UWB positioning system. *IEEE Radio and Wireless Symposium*, (pp. 55-58).
- Gabriel, S., Lau, R., & Gabriel, C. (1996). The dielectric properties of biological tissues: III parametric models for the dielectric spectrum of tissue. *Phys. Med. Biol.*, 41, 2271-2293.
- Gao, T., Pesto, C., Selavo, L., Chen, Y., Ko, J., Lim, J., et al. (2008). Wireless medical sensor networks in emergency response: implementation and pilot results. *IEEE International Conference on Technologies for Homeland Security*. Waltham, MA.
- Graichen, F., Arnold, R., Rohlmann, A., & Bergmann, G. (2007). Implantable 9-Channel Telemetry System for In Vivo Load Measurements With Orthopedic Implants. *IEEE transactions on biomedical engineering*, 54 (2), 253-261.
- Haider, M., Mahfouz, M., Islam, S., Eliza, S., Qu, W., & Pritchard, E. (2008). A low-power capacitance measurement circuit with high resolution and high degree of linearity. *51st Midwest Symp on Circuits and Systems*, (p. 261). Knoxville, TN.

- Healthcare, G. (n.d.). Retrieved from <http://www.gehealthcare.com>
- Iso-Ketola, P., Karinsalo, T., & Vanhala, J. (2008). HipGuard: A wearable measurement system for patients recovering from a hip operation. *2nd Intl Conf. on Pervasive Computing Tech. for Healthcare*. Tampere, Finland: PervasiveHealth 2008.
- Komarov, V., Wang, S., & Tang, J. (2005). Permittivity and measurements. In K. Chang (Ed.), *Wiley Encyclopedia RF Microwave Engineering* (pp. 3693-3711). New York: John Wiley & Sons.
- Kuhn, M., Mahfouz, M., Turnmire, J., Wang, Y., & Fathy, A. (Jan, 2011). A multi-tag access scheme for indoor UWB localization systems used in medical environments. *Proceedings of IEEE Topical Conference on Biomedical Wireless Technologies, Networks, and Sensing Systems (BioWireleSS)*, Phoenix, AZ, 75-78.
- Kuhn, M., Mahfouz, M., Zhang, C., Merkl, B., & Fathy, A. (2010). A system level simulation framework for UWB localization. *IEEE Transactions on Microwave Theory and Techniques*, 58 (12), Part 1, 3527-3537.
- Low, Z., Cheong, C., Ng, W., & Lee, Y. (2005). Pulse detection algorithm for line-of-sight (LOS) UWB ranging applications. *IEEE Ant. and Wireless Prop. Letters*, 4, 63-67.
- Mahfouz, M., Zhang, C., Merkl, B., Kuhn, M., & Fathy, A. (2008). Investigation of high accuracy indoor 3-D positioning using UWB technology. *IEEE Transactions on Microwave Theory and Techniques*, 56 (6), 1316-1330.
- Mahfouz, M., Kuhn, M., To, G., & Fathy, A. (2009). Integration of UWB and wireless pressure mapping in surgical navigation. *IEEE Transactions on Microwave Theory and Techniques*, 57 (10), Part 2, 2550-2564.
- Mahfouz, M., Kuhn, M. (Jan, 2011). UWB channel measurements and modeling for positioning and communications systems in the operating room. *Proceedings of IEEE Topical Conference on Biomedical Wireless Technologies, Networks, and Sensing Systems (BioWireleSS)*, Phoenix, AZ, 47-50.
- Mahfouz, M., Kuhn, M., Wang, Y., Turnmire, J., & Fathy, A. (Jan, 2011). Towards sub-millimeter accuracy in UWB positioning for indoor medical environments. *Proceedings of IEEE Topical Conference on Biomedical Wireless Technologies, Networks, and Sensing Systems (BioWireleSS)*, Phoenix, AZ, 47-50.
- McEwan, T. E. (2004). Patent No. 6,747,599. United States of America.
- Meier, C., Terzis, A., & Lindenmeier, S. (2007). A robust 3D high precision radio location system. *IEEE International Microwave Symp.*, (pp. 397-400).
- Meier, C., Terzis, A., & Lindenmeier, S. (2007). Investigation and suppression of multipath influence on indoor radio location in the millimeter wave range. *Conf. Wave Prop. Comm., Microwave Sys. Nav.*, (pp. 21-24). Chemnitz, Germany.
- Metronics. (n.d.). Retrieved from <http://www.medtronic.com/>
- Morris, S. J., & Paradiso, J. A. (2002). Shoe-integrated sensor system for wireless gait analysis and real-time feedback. *Proceedings of the 2nd Joint IEEE EMBS (Engineering in Medicine and Biology Society) and BMES (the Biomedical Engineering Society) Conference*.
- Mosshammer, R., Huener, M., Szumny, R., Kurekt, K., Hittner, J., & Gierlichli, R. (2007). A 5.8 GHz local positioning and communication system. *IEEE MTT-S International Microwave Symposium*, (pp. 1237-1240). Honolulu, USA.
- Myglucometer. (n.d.). Retrieved from <http://www.myglucometer.com/>
- Nelson, S. (1991). Dielectric properties of agricultural products - measurements and applications. *IEEE Trans. Elec. Insul*, 26 (5), 845-869.

- Nonin. (n.d.). Retrieved from <http://www.nonin.com/documents/M-5507%204000%20Cleveland%20Whitepaper.pdf>
- Omnipod. (n.d.). Retrieved from <http://www.myomnipod.com>
- Ossberger, G., Buchegger, T., Schimback, E., Stelzer, A., & Weigel, R. (2004). Non-invasive respiratory movement detection and monitoring of hidden humans using ultra wideband pulse radar. *IEEE International Conf UWB Sys. Tech.*, (pp. 395-399). Kyoto, Japan.
- Panasonic. (n.d.). Retrieved from <http://service.us.panasonic.com/OPERMANPDF/EW3153.PDF>
- Patel, S., Lorincz, K., Hughes, R., Huggins, N., Growden, J., Standaert, D., et al. (2009). Monitoring Motor Fluctuations in Patients With Parkinson's Disease Using Wearable Sensors. *IEEE Transactions on Information Technology in Biomedicine*, 13 (6).
- Pritchard, E., Mahfouz, M., Evans, B., Eliza, S., & Haider, M. (2008, Oct). Flexible capacitive sensors for high resolution pressure measurement. *IEEE sensors*, 1484.
- Public Domain Retrieved from <http://en.wikipedia.org/wiki/File:CapsuleEndoscope.jpg>
- Qu, W., Islam, S., Mahfouz, M., To, G., & Mofasta, S. (2010). Micro-cantilever Array Pressure Measurement System for Biomedical Instrumentation. *IEEE Sensors Journal*, 10 (2), 321-330.
- Qu, W., Islam, S., To, G., & Mahfouz, M. (2008). Design of analog signal processing integrated circuit for multi-channel biomedical strain measurement instrument. *International Conference on Biomedical Electronics and Devices*. Funchal, Portugal.
- Rohlmann, A., Gabel, U., Graichen, F., Bender, A., & Bergmann, G. (2007). An instrumented implant for vertebral body replacement that measures loads in the anterior spinal column. *Medical Engineering & Physics*, 29 (5), 580-585.
- Stelzer, A., Diskus, C., & Thim, H. (1999). A microwave position sensor with sub-millimeter accuracy. *47 (12)*, 2621-2624.
- Stelzer, A., Pourvoyeur, K., & Fischer, A. (2004). Concept and application of LPM-a novel 3-D local position measurement system. *IEEE Trans. Microwave Theory and Tech*, 52 (12), 2664-2669.
- SunTech. (n.d.). Retrieved from [www.suntechmed.com](http://www.suntechmed.com)
- To, G. (2007). *Development of the Telemetrical Intraoperative Soft Tissue Tension Monitoring System in Total Knee Replacement with MEMS and ASIC Technologies*. Knoxville, TN, USA: University of Tennessee.
- To, G., & Mahfouz, M. (2005). Development for Intra/Post Operative Surgical Instrument using MEMS/IC. *International Conference on Biomedical Engineering*. Singapore.
- To, G., Qu, W., & Mahfouz, M. (2006). ASIC Design for Wireless Surgical MEMS Device and Instrumentation. *IEEE EMBS*. New York, USA.
- Tragas, P., Kalis, A., Papadias, C., Ellinger, F., & Eickhoff, R. (2007). RESOLUTION: reconfigurable systems for mobile local communication and positioning. *Mob. and Wireless Comm. Summit*, (pp. 1-5). Budapest, Hungary.
- Ubisense. (2011). Retrieved from [www.ubisense.net](http://www.ubisense.net)
- Vorst, A.V., Rosen, A., & Kotsuka, Y. (2006). *RF/Microwave Interaction with Biological Tissues*, John Wiley & Sons Inc., ISBN: 9780471732778, Hoboken, NJ.

- Waldmann, R., Weigel, P., & Gulden, P. (2008). Method for high precision local positioning radar using an ultra wideband technique. *International Microwave Symp*, (pp. 117-120). Atlanta, USA.
- Zebra Enterprise Solutions (2011). Retrieved from [http://www.zebra.com/id/zebra/na/en/index/products/location/ultra\\_wideband.html](http://www.zebra.com/id/zebra/na/en/index/products/location/ultra_wideband.html).
- Zetik, J., Sachs, J., & Thomä, R. (2004). UWB localization - active and passive approach. *Proceedings of the 21st IEEE IMTC*, 2, pp. 1005-1009.
- Zhang, C., Fathy, A., & Mahfouz, M. (2007). Performance enhancement of a sub-sampling circuit for ultra-wideband signal processing. *IEEE Micro. and Wireless Comp. Lett* , 17 (2), 873-875.
- Zhang, C., Kuhn, M., Merkl, B., Fathy, A., & Mahfouz, M. (2010). Real-time non-coherent UWB positioning radar with millimeter range accuracy: theory and experiment. *IEEE Transactions on Microwave Theory and Techniques* , 58 (1), 9-20.



## **Novel Applications of the UWB Technologies**

Edited by Dr. Boris Lembrikov

ISBN 978-953-307-324-8

Hard cover, 440 pages

**Publisher** InTech

**Published online** 01, August, 2011

**Published in print edition** August, 2011

Ultra wideband (UWB) communication systems are characterized by high data rates, low cost, multipath immunity, and low power transmission. In 2002, the Federal Communication Commission (FCC) legalized low power UWB emission between 3.1 GHz and 10.6 GHz for indoor communication devices stimulating rapid development of UWB technologies and applications. The proposed book *Novel Applications of the UWB Technologies* consists of 5 parts and 20 chapters concerning the general problems of UWB communication systems, and novel UWB applications in personal area networks (PANs), medicine, radars and localization systems. The book will be interesting for engineers and researchers occupied in the field of UWB technology.

### **How to reference**

In order to correctly reference this scholarly work, feel free to copy and paste the following:

Mohamed Mahfouz, Michael Kuhn and Gary To (2011). The Future of Ultra Wideband Systems in Medicine: Orthopedic Surgical Navigation, *Novel Applications of the UWB Technologies*, Dr. Boris Lembrikov (Ed.), ISBN: 978-953-307-324-8, InTech, Available from: <http://www.intechopen.com/books/novel-applications-of-the-uw-technologies/the-future-of-ultra-wideband-systems-in-medicine-orthopedic-surgical-navigation>

# **INTECH**

open science | open minds

### **InTech Europe**

University Campus STeP Ri  
Slavka Krautzeka 83/A  
51000 Rijeka, Croatia  
Phone: +385 (51) 770 447  
Fax: +385 (51) 686 166  
[www.intechopen.com](http://www.intechopen.com)

### **InTech China**

Unit 405, Office Block, Hotel Equatorial Shanghai  
No.65, Yan An Road (West), Shanghai, 200040, China  
中国上海市延安西路65号上海国际贵都大饭店办公楼405单元  
Phone: +86-21-62489820  
Fax: +86-21-62489821

© 2011 The Author(s). Licensee IntechOpen. This chapter is distributed under the terms of the [Creative Commons Attribution-NonCommercial-ShareAlike-3.0 License](#), which permits use, distribution and reproduction for non-commercial purposes, provided the original is properly cited and derivative works building on this content are distributed under the same license.